

INFORMATION TO USERS

This manuscript has been reproduced from the microfilm master. UMI films the text directly from the original or copy submitted. Thus, some thesis and dissertation copies are in typewriter face, while others may be from any type of computer printer.

The quality of this reproduction is dependent upon the quality of the copy submitted. Broken or indistinct print, colored or poor quality illustrations and photographs, print bleedthrough, substandard margins, and improper alignment can adversely affect reproduction.

In the unlikely event that the author did not send UMI a complete manuscript and there are missing pages, these will be noted. Also, if unauthorized copyright material had to be removed, a note will indicate the deletion.

Oversize materials (e.g., maps, drawings, charts) are reproduced by sectioning the original, beginning at the upper left-hand corner and continuing from left to right in equal sections with small overlaps. Each original is also photographed in one exposure and is included in reduced form at the back of the book.

Photographs included in the original manuscript have been reproduced xerographically in this copy. Higher quality 6" x 9" black and white photographic prints are available for any photographs or illustrations appearing in this copy for an additional charge. Contact UMI directly to order.

UMI

A Bell & Howell Information Company
300 North Zeeb Road, Ann Arbor, MI 48106-1346 USA
313/761-4700 800/521-0600

**VIBRATION AS AN AID
IN ROBOTIC PEG-IN-HOLE ASSEMBLY**

**by
Hsin-Te Liao**

**A Dissertation
Submitted to the Faculty of
New Jersey Institute of Technology
in Partial Fulfillment of the Requirements for the Degree of
Doctor of Philosophy**

Department of Mechanical Engineering

October 1995

UMI Number: 9605745

**Copyright 1995 by
Liao, Hsin-Te
All rights reserved.**

**UMI Microform 9605745
Copyright 1995, by UMI Company. All rights reserved.**

**This microform edition is protected against unauthorized
copying under Title 17, United States Code.**

UMI

**300 North Zeeb Road
Ann Arbor, MI 48103**

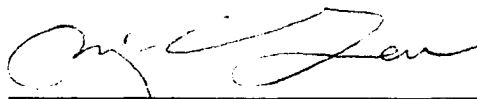
Copyright © 1995 by Hsin-Te Liao

ALL RIGHTS RESERVED

APPROVAL PAGE

VIBRATION AS AN AID
IN ROBOTIC PEG-IN-HOLE ASSEMBLY

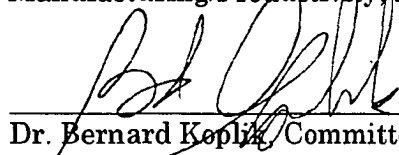
Hsin-Te Liao



Aug. 10, 1995

Dr. Ming-C. Leu, Dissertation Advisor
Professor of Mechanical Engineering and State Chair in
Manufacturing/Productivity, NJIT

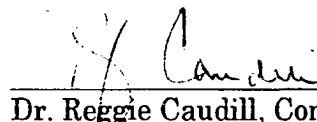
Date



Aug 10, 1995

Dr. Bernard Koplik, Committee Member
Professor of Mechanical Engineering and Chairperson of the
Department of Mechanical Engineering, NJIT

Date



8/18/95

Dr. Reggie Caudill, Committee Member
Professor of Industrial and Manufacturing Engineering and
Executive Director of the Center for Manufacturing Systems, NJIT

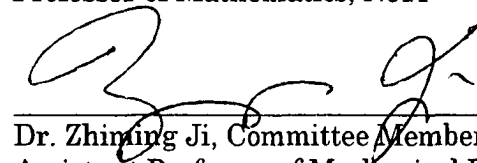
Date



8/10/95

Dr. Denis Blackmore, Committee Member
Professor of Mathematics, NJIT

Date



Aug. 10, 95

Dr. Zhiming Ji, Committee Member
Assistant Professor of Mechanical Engineering, NJIT

Date

ABSTRACT

VIBRATION AS AN AID IN ROBOTIC PEG-IN-HOLE ASSEMBLY

**by
Hsin-Te Liao**

This dissertation presents an analytical and experimental investigation of vibration assisted engagement for parts mating. A dynamic model of assembly is established by using Lagrange's equation for impact to derive impact equations for a robotic manipulator in peg-in-hole assembly. The model can be used to analyze part motion and contact force in the mating of parts by robots. The impact equations of a SCARA robot are derived using this model and utilized to investigate how robot configuration, insertion speed, chamfer angle, coefficient of restitution and other system parameters affect impulsive force and departure angle in the assembly of a peg with a chamfered hole in the presence of position errors. In the analytical investigation, how the vibration amplitude, vibration frequency, frequency ratio, phase angle, uncertainty and tolerance of the assembly system affect the engagement time is analyzed. An algorithm is developed to determine the required time for engagement given a set of assembly and vibration parameters. An intelligent force-based approach is used in conjunction with this algorithm to aid mating of parts and is implemented in experiments to verify analytical results.

BIOGRAPHICAL SKETCH

Author: Hsin-Te Liao

Degree: Doctor of Philosophy

Date: October 1995

Date of Birth: September 6, 1959

Place of Birth: Taiwan, Republic of China

Undergraduate and Graduate Education

- Doctor of Philosophy in Mechanical Engineering
New Jersey Institute of Technology,
Newark, New Jersey, 1995
- Master of Science in Mechanical Engineering
New Jersey Institute of Technology,
Newark, New Jersey, 1986
- Diploma in Mechanical Engineering
Ming-Chi Institute of Technology
Taipei, Taiwan, 1980

Major: Mechanical Engineering

Presentation and Publications:

Liao, Hsin-Te, and Leu, Ming. C., 1994, "Impact Model for Robotic Peg-in-Hole Assembly," The Third International Conference on Automation Technology, Taipei, R.O.C., Vol. 5, pp. 259-266.

Liao, Hsin-Te, 1993, "Impact Model for the Peg-in-Hole Assembly," Presented in Polytechnic University, Brooklyn, New York, at the Third ASME Regional II Graduate Student Technical Conference.

Liao, Hsin-Te, 1990, "Surface Stresses Analysis of Thin-Wall Pressure Vessels by the computer," The 5th T.V.E. Conference of R.O.C., pp. 4247-4257.

Liao, Hsin-Te, *Strength of Materials*, 1989, Taipei: Dahyun Publishers, Chinese Edition.

**This dissertation is dedicated to
my parents
my lovely wife, Yean-Seng Chang
and my son, Ryan Liao**

ACKNOWLEDGMENT

The author will always remain indebted to his advisor, Professor Ming Leu, for his ever present guidance and support, both technical and interpersonal, throughout this research.

Thanks are due to Professors Bernard Koplik, Reggie Caudill, Denis Blackmore, and Zhiming Ji for dedicating their time to serve as members of the committee.

The author is grateful to Professors Ronyaw Chen for graduate advice and assistance throughout these years.

The author also appreciates the staff in the Department of Mechanical Engineering: Don Rosander, Jack Gidney and Eddings Marcia for their time-to-time assistance.

Timely help and suggestions came from many good friends Dr. Shu-Chieh Chang, Dr. Yeou-Kai Wu, Dr. Hermean Wong, Wenlong Yao and Chin Chan.

The author is grateful to the members of his family, especially his father who died during his doctorate research, for their love, faith, and patience.

Lastly, the author would like to express his greatest and deepest gratitude to his lovely wife, Yean-Seng Chang, for the many courage and sacrifices she has made.

TABLE OF CONTENTS

Chapter	Page
1. INTRODUCTION.....	1
1.1 Motivation and Significance.....	1
1.2 Literature Survey.....	2
1.3 Objective and Scope of Research.....	6
1.4 Outline of Dissertation.....	7
2. IMPACT EQUATION FOR ROBOTIC PEG-IN-HOLE ASSEMBLY.....	8
2.1 Impact Force and Part Motion After Impact.....	8
2.2 Impact Equation for a General Manipulator.....	9
2.3 Procedure of Deriving Impact Equations.....	12
2.4 Assembly by SCARA-Type Robot.....	13
2.5 Effect of Parameters on Impulse and Departure Angle.....	25
3. EFFECT OF VIBRATION PARAMETERS ON ENGAGEMENT TIME.....	41
3.1 Introduction.....	41
3.2 Positional Uncertainty and Tolerance.....	43
3.3 Vibration Amplitude.....	45
3.4 Vibration Frequency.....	46
3.5 Algorithm for Determining Required Sweep Time.....	49
3.6 Numerical Results and Discussion.....	52

TABLE OF CONTENTS
(Continue)

Chapter	Page
4. EXPERIMENTAL INVESTIGATION OF PEG-IN-HOLE INSERTION.....	60
4.1 Introduction.....	60
4.2 Experimental Setup.....	60
4.3 Practical Problems Encountered.....	61
4.4 Algorithm of Engagement Process.....	65
4.5 Experiments of Peg-in-Hole Insertion.....	68
4.6 Effect of Vibration Parameters on Contact Force.....	74
5. CONCLUSION.....	80
APPENDIX A TIME HISTORIES OF FORCE AND MOMENT OF CONTACT IN THE MATING EXPERIMENT.....	82
REFERENCES.....	87

LIST OF TABLES

Table	Page
2.1 Denevit-Hartenberg parameters of a SCARA-type robot.....	14
2.2 Nominal values of link parameters of a SCARA-type robot.....	29
3.1 Dimensions of the peg and hole piece.....	53

LIST OF FIGURES

Figure	Page
1.1 Model of peg-in-hole insertion.....	2
2.1 Model of robotic peg-in-hole assembly.....	10
2.2 SCARA-type robot with three revolute and one prismatic joints.....	13
2.3 Impact coordinate frame.....	14
2.4 Transformation from impact coordinate frame to end-effector coordinate frame.....	15
2.5 Shape and dimension of link 1.....	17
2.6 Shape and dimension of link 2.....	18
2.7 Shape and dimension of link 3 and 4.....	19
2.8 The departure angle and chamfer angle.....	25
2.9 Normal impulse vs. coefficient of restitution and chamfer angle.....	30
2.10 Departure angle vs. coefficient of restitution and chamfer angle.....	30
2.11 Normal impulse vs. coefficient of friction and chamfer angle.....	31
2.12 Departure angle vs. coefficient of friction and chamfer angle.....	31
2.13 Normal impulse vs. insertion speed and chamfer angle.....	32
2.14 Departure angle vs. insertion speed and chamfer angle.....	33
2.15 Normal impulse vs. joint 1 and 2 angles.....	34
2.16 Departure angle vs. joint 1 and 2 angles	34
2.17 Normal impulse vs. joint 2 and 3 angles	35
2.18 Departure angle vs. joint 2 and 3 angles	35

**LIST OF FIGURES
(Continue)**

Figure	Page
2.19 Normal impulse vs. joint 2 and 4 angles	36
2.20 Departure angle vs. joint 2 and 4 angles	36
2.21 Normal impulse vs. mass and length of link 1.....	37
2.22 Departure angle vs. mass and length of link 1.....	38
2.23 Normal impulse vs. mass and length of link 2.....	38
2.24 Departure angle vs. mass and length of link 2.....	39
2.25 Normal impulse vs. mass and radius of link 3.....	39
2.26 Normal impulse vs. mass and radius of link 3.....	40
3.1 Increasing-amplitude vibration.....	41
3.2 Constant-amplitude vibration.....	42
3.3 Two possible relations between uncertainty set U and tolerance set T.....	44
3.4 Sizes of uncertainty set U and tolerance set T.....	45
3.5 Sliding motion on chamfer surface.....	47
3.6 Sweep path for helping engagement.....	50
3.7 Sampling point of sweep path.....	52
3.8 Sweep time vs. frequency ratios and phase angles.....	53
3.9 Sweep time vs. frequency ratios and phase angles.....	54
3.10 Sweep time vs. frequency ratios and phase angles.....	55

LIST OF FIGURES
(Continue)

Figure	Page
3.11 Sweep time vs. frequency ratios and phase angles ($U_x^1 = U_x^2 = U_y^1 = U_y^2 = 5.33$ mm)	56
3.12 Sweep time vs. frequency ratios and ratios of uncertainty to tolerance.....	57
3.13 Sweep paths for different frequency ratios.....	58
4.1 Setup for vibration-assisted mating of parts with Adept-1 robot.....	61
4.2 Model of problem 1.....	62
4.3 Model of problem 2.....	63
4.4 Flowchart of peg-in-hole insertion.....	65
4.5 Determination of the amount of downward motion of the robot.....	68
4.6 Location of initial contact points.....	69
4.7 Forces with initial position at point 5.....	70
4.8 Moments with initial position at point 5.....	71
4.9 Forces with initial position at point 3.....	72
4.10 Moments with initial position at point 3.....	73
4.11 Forces with initial position at point 8.....	73
4.12 Moments with initial position at point 8.....	74
4.13 Contact forces with $A = B = 4$ mm and $\omega = 6$ rad./sec	75
4.14 Contact forces with $A = B = 4$ mm and $\omega = 5$ rad./sec	75
4.15 Contact forces with $A = B = 4$ mm and $\omega = 4$ rad./sec	76

LIST OF FIGURES
(Continue)

Figure	Page
4.16 Contact forces with $A = B = 8$ mm and $\omega = 6$ rad./sec	77
4.17 Contact forces with $A = B = 8$ mm and $\omega = 5$ rad./sec	78
4.18 Contact forces with $A = B = 4$ mm and $\omega = 4$ rad./sec	78
A.1 Forces with initial position at point 1.....	82
A.2 Moments with initial position at point 1.....	82
A.3 Forces with initial position at point 7.....	83
A.4 Moments with initial position at point 7.....	83
A.5 Forces with initial position at point 6.....	84
A.6 Moments with initial position at point 6.....	84
A.7 Forces with initial position at point 2.....	85
A.8 Moments with initial position at point 2.....	85
A.9 Forces with initial position at point 4.....	86
A.10 Moments with initial position at point 4.....	86

NOMENCLATURE

- A, B** vibration amplitude
- a_i** length of link i
- a_g** length of peg
- c** clearance ratio
- C_t** center of tolerance area
- [C]** matrix of effective compliance at the peg's tip
- d_i** distance in z direction between coordinate frame x_i - y_i - z_i and x_{i-1} - y_{i-1} - z_{i-1}
- \dot{d}_3** velocity of joint 3 before impact
- \dot{d}'_3** velocity of joint 3 after impact
- d_x** distance in x direction between the center of the peg and the location of the contact point
- d_y** distance in y direction between the center of the peg and the location of the contact point
- e** coefficient of restitution
- F_x** insertion force in the x direction
- F_y** insertion force in the y direction
- F_z** insertion force in the z direction
- $F_{z,s}$** difference between the largest and smallest value of the insertion force F_z during sweep

NOMENCLATURE (Continue)

f_x	contact force in the x direction
f_y	contact force in the y direction
f_z	contact force in the z direction
$[f]$	vector of external force acting on the peg's tip
\bar{G}	angular moment impulse vector
H_i	generalized impulse associated with coordinate frame x_i - y_i - z_i
h_i	height of link i (chapter 2)
h_1	amount of move-up displacement to reduce contact force
h_2	amount of move-down displacement to detect whether the peg lies within the hole or not
h_t	amount below the top surface of the hole piece
I_j	motor inertia of link j
J_i	inertia matrix of link i
K	kinetic energy
k	ratio of frequencies
m_i	mass of link i (chapter 2)
m_{i1}	mass of part A in link i
m_{i2}	mass of part B in link i
m_{i3}	mass of part C in link i
m_x	moment in x direction (chapter 3 and 4)

NOMENCLATURE (Continue)

m_y	moment in y direction (chapter 3 and 4)
m_z	moment in z direction (chapter 3 and 4)
n	number of degrees of freedom (chapter 2)
n	number of lines that divided uncertainty area in x direction (chapter 3)
P_x	impulse in x direction
P_y	impulse in y direction
P_z	impulse in z direction
q_j	location of joint j
\dot{q}_j	velocity of joint j at the beginning of impact
\dot{q}'_j	velocity of joint j at the end of impact
\vec{P}	linear force impulse vector
${}^{j-1}R_e$	rotation matrix from end-effector coordinate frame to coordinate frame of link j
eR_p	rotation matrix from impulse coordinate frame, n-t-t', to end-effector coordinate frame $x_e-y_e-z_e$
s	sweep path
r_i	radius of link i
\vec{r}_j	vector corresponding to the last column of ${}^{j-1}T_j$
T	tolerance box

NOMENCLATURE (Continue)

T_x ,	tolerance in x direction
T_y	tolerance in y direction
${}^{i-1}T_i$	homogeneous transformation matrix from coordinate frame i to i-1 (chapter 2)
t_d	delay time of hardware response
U	uncertainty box
U_x ,	uncertainty in x direction
U_y	uncertainty in y direction
\hat{u}_j	unit vector along z_{j-1} (i.e. axis of joint j)
v_i	insertion speed
v'	velocity of the peg's tip after impact
v_n	normal velocity of the peg's tip
v_t	tangential velocity of the peg's tip
v'_n	normal velocity of the peg's tip after impact
v'_t	tangential velocity of the peg's tip after impact
v_l	maximum lateral speed of vibration motion
w	chamfer width
Δ	change over time interval of impact (chapter 2)
Δt	time increment

NOMENCLATURE (Continue)

α	chamfer angle
$[\delta]$	vector of deflection at the peg's tip
ϕ	location of the contact point on the peg
γ	departure angle
μ	coefficient of friction along chamfer surface
θ	phase angle (chapter 3)
θ_i	angle of joint i (chapter 2)
$\dot{\theta}_i$	velocity of joint i before impact
$\dot{\theta}'_i$	velocity of joint i after impact
ω	vibration frequency
ω_n	nature frequency of robot system
Θ	set difference

CHAPTER 1

INTRODUCTION

1.1 Motivation and Significance

Assembly is an important part of manufacturing. Robotic assembly is representative of a class of tasks in which contact occurs in the robot operation. In high-speed assembly a robot arm dynamically interacts with a workpiece, where an impulsive force is generated and exerted on the end-effector of the robot. This impact may damage the mating parts or change the motion of the robot. To accomplish such high-speed assembly, the dynamic response of the robot arm must be investigated in order to accommodate or control the robot's interaction with the workpiece. Mating of two parts, which can often be modeled as a peg-in-hole insertion problem, is a typical robotic assembly operation. Because of the substantial positional and dimensional errors in assembly machines, parts, fixtures, etc., positional uncertainty between two mating parts is inevitable, as shown in Figure 1-(a). Engagement failure is defined as the situation where two mating parts cannot engage after they come in contact with each other. In addition to engagement failure, there is another kind of assembly failure called insertion failure, where wedging or jamming occurs during the insertion process, after

the parts have engaged. Both engagement failure and insertion failure are commonly encountered in parts mating.

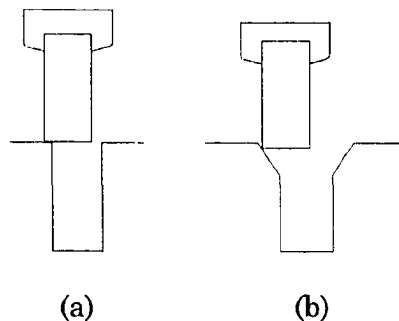


Figure 1.1 Model of peg-in-hole insertion

1.2 Literature Survey

Considerable research and development efforts have been made on parts mating. The main research activities include four main directions: parts mechanics, feedback control, auxiliary device design, and vibration assisted parts mating. The mechanics of parts mating was studied extensively at Charles Stark Drapers Laboratory (Simunovic, 1975; Drake, 1977; Whitney, 1982; Gustavson, 1985; Whitney and Rourke, 1986; Nevins and Whitney, 1989) and elsewhere. Simunovic investigated force information in robotic peg-in-hole insertion, which was further developed into the jamming and wedging diagrams in Whitney's work (1979, 1982). The result of this analysis was used to design a remote center compliance (RCC) device, a passive wrist which provides some compliance to absorb the misalignment between the mating parts. Incorporated with a chamfer surface, the RCC can guide the

peg into the hole as shown in Figure 1-(b). The RCC device has been demonstrated to be highly effective in avoiding insertion failure. However, for the RCC device to be effective the peg must fall within the chamfer mouth at the first contact. Furthermore, if the initial angular error is too large, wedging will occur and cannot be overcome with RCC. There were many other studies on analysis of parts mating and strategies for automated assembly. Ohwovoriole and Roth (1981) used the theory of screws to study 3-D parts mating. Sturges (1988) constructed general 3-D models for assembly of non-axisymmetric parts and used them to analyze mating of rectangular parts. Cutkosky and Kao (1989) used properties of the grasp stiffness matrix to determine whether a grasp is stable or not. Pai and Leu (1991) derived a sufficient condition on the joint stiffness of a robot for jamming prevention. Leu and Jia (1995), following an analysis similar to Whitney's, derived the mating force and part movement in peg-in-hole assembly by an industrial robot with its own compliance. In that case the end-effector compliance matrix is a general matrix, not a diagonal matrix.

Strategies for compliant assembly have been studied by a number of researchers. Lozano-Perez, et al. (1981) developed a method of synthesizing fine motion strategies. Mason (1981) developed a theory of compliance and force control based on models of the manipulator and task geometry. Donald (1988) developed a formal framework for error detection and recovery using geometric characterization. Lee and Hou (1988) presented an approach for

automatically determining the C-frame for various shaped objects in peg-in-hole assembly. Gottschlich and Kak (1989) discussed a dynamic planning strategy capable of detecting and recovering errors during an assembly process. Caine et al. (1989) developed strategies for chamferless insertion of axisymmetric and non-axisymmetric parts. Peshkin (1990) proposed a method for synthesizing an assembly task by specifying a compliance matrix which is error corrective. McCarragher and Asada (1992) developed a discrete event controller using Petri net modeling to determine the optimal sequence of discrete states for successful assembly.

Another approach to overcome positional errors in assembly is using feedback control techniques to perform on-line correction of positional errors. Raibert and Craig (1982) were among the first to propose a hybrid position/force control technique for controlling compliant motions of a manipulator. The goal of the control was to simultaneously satisfy position and force constraints. Hogan (1985) devised a method of impedance control which was capable of accepting positions and outputting forces. Kelly (1990) developed a controller which was based on fuzzy logics to interpret the forces and torques generated by the wrist-mounted force-torque sensor during the insertion process. Hara and Yokogawa (1991) dealt with a precision inserting operation for chamferless parts under vague positional information by using approximate reasoning. The position of the parts was recognized by introducing two fuzzy sets. Ji and Leu (1992) used visual measurement and

feedback techniques to perform on-line error correction. It involved the use of a vision camera to probe the part position, with the sensed data fed back to the monitor controller.

In high-speed assembly, Asada and Kakumoto (1987,1988,1990) used the concept of virtual mass and generalized centroid to analyze the dynamic insertion process and designed a dynamic RCC. Keller (1986) presented a theory of impact of two rigid bodies, taking account of friction. Wang and Mason (1987) developed graphic methods to analyze the resultant motions of two objects under impact. McCarragher and Asada (1993) presented a model-based approach to study the dynamics generated due to geometric interactions in an assembly process. Youcef-Toumi and Gutz (1994) showed that tracking of impact force could be tuned by selecting a favorable dimensionless ratio of force to approach velocity. These studies have revealed that it is important to take dynamic forces into consideration in the assembly analysis when the speed of assembly is high.

An interesting approach to aid parts mating is to apply vibration in order to increase the tolerance of the assembly system for positional uncertainty in the mating parts, without the use of sensory feedback and compliant devices. A study at AT&T Bell Laboratory (1984) demonstrated that applying vibrational motions provided a means for solving the problem of parts misalignment in printed wiring board assembly. The experimental results indicated that proper vibrational frequencies and amplitudes could

help parts engagement by creating relative motions between the mating parts. Jeong and Cho (1989) designed a pneumatic device to generate vibrations and discussed the effect of vibration frequencies in vibration assisted assembly. Mohri (1988), at Toyota Technology Institute, showed that insertion failure could be eliminated by introducing ultrasonic vibration to reduce the contact friction. Leu and Liu (1991) did a quasi-static analysis of force and motion for vibration-assisted insertion. Li and Asada (1992) presented an experiment-based approach using the Taguchi Method applied to the turning of the vibrator. The vibration was produced so that the effect of friction and stick-slip could be minimized. Leu and Katz (1994) determined the amplitude and cycle requirements for feasible parts mating with the aid of an increasing-amplitude vibration.

1.3 Objective and Scope of Research

The main objective of this research is to provide knowledge toward a full understanding about how vibration affects mating of parts and how to properly select vibration parameters for optimal assembly results. The research is focused on the engagement phase of parts mating. A mathematical model is established to analyze contact forces and part motions after the mating parts contact each other. An algorithm is developed to determine the optimal amplitudes, frequency, frequency ratio, and phase angle for different tolerances and uncertainties of the assembly system.

Experiments of peg-in-hole insertion are performed to verify the theoretical results. A force-based intelligent approach is used to solve some practical problems such as the flatness and levelness of mating parts and response delay of signal communication which may cause insertion failure. An experimental investigation of how vibration amplitude and vibration frequency affect the insertion force in constant-amplitude vibrations is also described.

1.4 Outline of Dissertation

In chapter 2, Lagrange's equation for impact is used to derive the impact equation for a general manipulator. The details of the derivation of the robot impact equation are given. A SCARA robot is used as an example to illustrate how robotic assembly parameters affect impact force and part motion. In chapter 3, selection of suitable vibration parameters is discussed. An algorithm to determine minimum sweep time for various ratios of uncertainty to tolerance is also developed. In chapter 4 a force-based intelligent approach is used to aid mating of parts in our experiments to verify analytical results. Conclusions are given in chapter 5.

CHAPTER 2

IMPACT EQUATION FOR ROBOTIC PEG-IN-HOLE ASSEMBLY

2.1 Impact Force and Part Motion After Impact

In the peg-in-hole insertion, an impact force is produced at the point of contact as the peg contacts the chamfer wall or surface of the hole piece. This impact force will change the part motion and may cause assembly failure or damage the mating parts. Some robots such as the Adept One will shut off the power in order to protect the robot if the contact force is too large. It is important to analyze the impact force and part motion after contact and during engagement in order to adopt a suitable control strategy and select optimal assembly parameters. The following Lagrange's equation for collision (Goldsmith, 1959) is used to derive the general form of impact equation for a manipulator colliding with a workpiece:

$$\Delta \left(\frac{\partial K}{\partial \dot{q}_i} \right) = H_i \quad i=1,2,\dots,n \quad (2.1)$$

where

q_i : generalized coordinate

\dot{q}_i : generalized velocity

K : kinetic energy

H_i : generalized impulse

n : number of degrees of freedom

Δ : change over time interval of impact

The Lagrange's equation for impact does not include potential energy. This is due to the fundamental assumption of rigid body impact that the position coordinates remain unchanged during impact.

From the set of impact equations together with the coefficient of restitution and coefficient of friction, the impulse and part motion after collision can be analyzed. If the duration of impact is known, the impact force can be easily calculated from the obtained impulse. Goldsmith (1959) described how to set up experiments to measure the coefficient of restitution and the duration of impact.

2.2 Impact Equation for a General Manipulator

The peg-in-hole assembly by a general manipulator is modeled as shown in Figure 3.1 where $n-t-t'$ is the impact coordinate frame. There are six components of the impulsive force and moment at the contact point. The hole piece is assumed to be rigid. The impact equations can be derived for the assembly by applying equation (2.1) as follows:

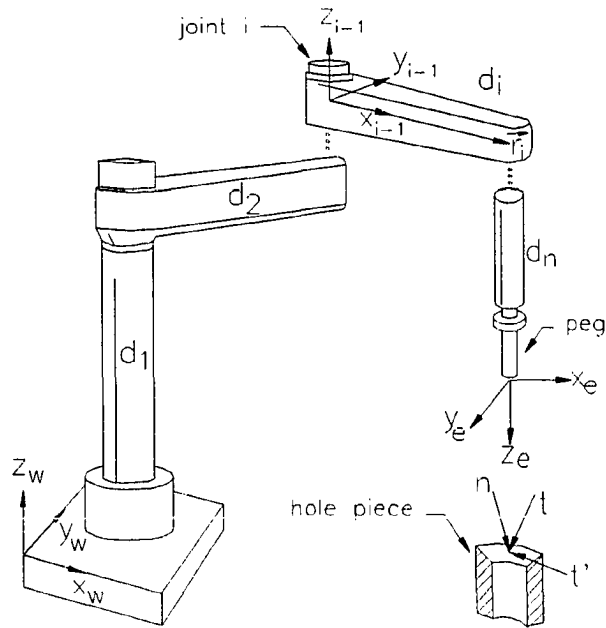


Figure 2.1 Model of robotic peg-in-hole assembly

The total kinetic energy of the manipulator is:

$$K = \frac{1}{2} \sum_{i=1}^n \sum_{p=1}^i \sum_{k=1}^i \text{Trace} \left(\frac{\partial \mathbf{T}_i}{\partial \mathbf{q}_p} \mathbf{J}_i \frac{\partial \mathbf{T}_i^T}{\partial \mathbf{q}_k} \right) \dot{\mathbf{q}}_p \mathbf{q}_k + \frac{1}{2} \sum_{i=1}^n \mathbf{I}_i \dot{\mathbf{q}}_i^2 \quad (2.2)$$

The derivative of the kinetic energy associated with joint j is

$$\frac{\partial K}{\partial \dot{\mathbf{q}}_j} = \sum_{i=1}^n \sum_{k=1}^i \text{Trace} \left(\frac{\partial \mathbf{T}_i}{\partial \mathbf{q}_j} \mathbf{J}_i \frac{\partial \mathbf{T}_i^T}{\partial \mathbf{q}_k} \right) \dot{\mathbf{q}}_k + \mathbf{I}_j \dot{\mathbf{q}}_j \quad j = 1, 2, \dots, n \quad (2.3)$$

Thus

$$\Delta \left(\frac{\partial K}{\partial \dot{q}_j} \right) = \sum_{i=1}^n \sum_{k=1}^i \text{Trace} \left(\frac{\partial T_i}{\partial q_j} J_i \frac{\partial T_i^T}{\partial q_k} \right) (\dot{q}'_k - \dot{q}_k) + I_j (\dot{q}'_j - \dot{q}_j) \quad j = 1, 2, \dots, n \quad (2.4)$$

The generalized impulse H_j associated with joint j can be obtained by applying the principle of virtual work (Huang 1967) as follows:

$$H_j = \begin{cases} \left(\bar{r}_j \times {}^{j-1}R_e {}^eR_p \bar{P} \right) \cdot \hat{u}_j + {}^{j-1}R_e {}^eR_p \bar{G} \cdot \hat{u} & \text{for a revolute joint} \\ {}^{j-1}R_e {}^eR_p \bar{P} \cdot \hat{u}_j & \text{for a prismatic joint} \end{cases} \quad (2.5)$$

Substituting Equation (2.4) and (2.5) into (2.1) leads to

$$\begin{aligned} & \sum_{i=1}^n \sum_{k=1}^i \text{Trace} \left(\frac{\partial T_i}{\partial q_j} J_i \frac{\partial T_i^T}{\partial q_k} \right) (\dot{q}'_k - \dot{q}_k) + I_j (\dot{q}'_j - \dot{q}_j) \\ & = \begin{cases} \left(\bar{r}_j \times {}^{j-1}R_e {}^eR_p \bar{P} \right) \cdot \hat{u}_j + \left({}^{j-1}R_e {}^eR_p \bar{G} \right) \cdot \hat{u} & \text{for a revolute joint} \\ \left({}^{j-1}R_e {}^eR_p \bar{P} \right) \cdot \hat{u}_j & \text{for a prismatic joint} \end{cases} \end{aligned} \quad (2.6)$$

where

\dot{q}_j : velocity of joint j at the beginning of impact

\dot{q}'_j : velocity of joint j at the end of impact

T_i : homogeneous transformation matrix of link i

J_i : inertia matrix of link i

I_j : motor inertia of link j

$\bar{P} = [P_n \quad P_t \quad P_v]^T$: linear force impulse vector

$\bar{G} = [G_n \quad G_t \quad G_v]^T$: angular moment impulse vector

${}^{j-1}R_o$: rotation matrix from end-effector coordinate frame to coordinate frame of link j

oR_p : rotation matrix from impulse coordinate frame, n-t-t', to end-effector coordinate frame, x_e - y_e - z_e (Figure 2.1)

\bar{r}_j : vector corresponding to the last column of ${}^{j-1}T_j$

\hat{u}_j : unit vector along z_{j-1} (i.e. axis of joint j)

The above impact equations have n equations but n+6 unknowns, which are n joint velocities after impact and six impulse components. Therefore, six more equations are needed to solve for these unknowns. These six equations can be obtained from the definitions of coefficients of restitution and friction (Brach, 1989).

2.3 Procedure of Deriving Impact Equations

The procedure of deriving impact equations for a particular manipulator is as follows:

1. Define the coordinates of each joint.
2. Establish Denevit-Hartenberg parameters of robot links.
3. Find homogeneous transformation matrices T_1, T_2, \dots, T_n .
4. Obtain the change of the derivative of kinetic energy associated with each joint, i.e., $\Delta\left(\frac{\partial K}{\partial q_i}\right)$, using Equation (2.4).
5. Find the rotation matrix from the impact coordinate frame to the end effector coordinate frame, oR_p .
6. Find the general impulse H_i using Equation (2.5).

7. Form $\Delta \left(\frac{\partial K}{\partial q_i} \right) = H_i$.
8. Find the normal velocity at the surface contact. Then relate the normal velocities at the beginning and the end of impact by the coefficient of restitution.
9. Relate the tangential impulse with the normal impulse with the coefficient of friction.

2.4 Assembly by SCARA-Type Robot

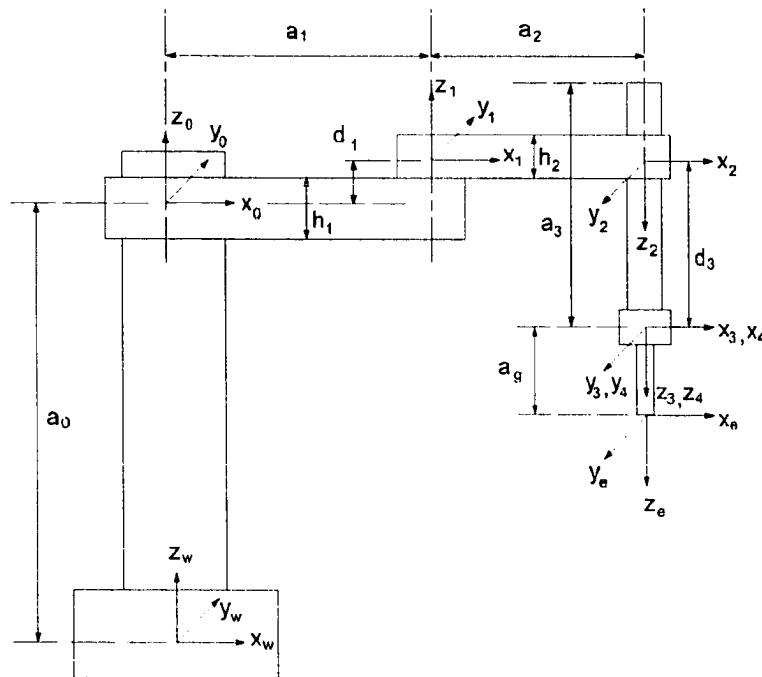


Figure 2.2 SCARA-type robot with three revolute and one prismatic joints

A SCARA-type robot with three revolute joints and one prismatic joint as shown in Figure 2.2 is used as an example to demonstrate the procedure in Section 2.3 for deriving the impact equations. Joints 1, 2, and 4 of the robot

are revolute joints and joint 3 is a prismatic joint. We will later examine how the manipulator parameters affect the impulse and part motion after impact.

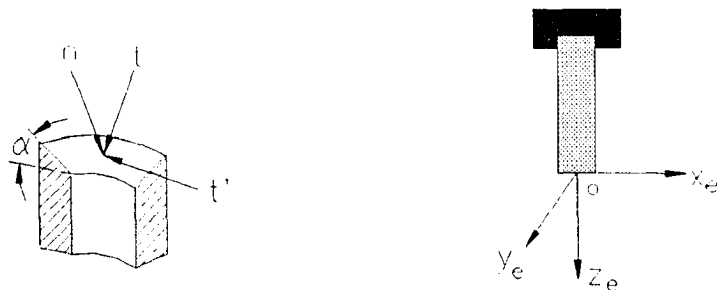
The Denevit-Hartenberg parameters of the robot links are shown in Table 2.1.

Table 2.1 Denevit-Hartenberg parameters of a SCARA-type robot

link #	α_i	a_i	d_i	θ_i
1	0	a_1	d_1	θ_1
2	180°	a_2	0	θ_2
3	0	0	d_3	0
4	0	0	0	θ_4

The transformation matrix from the base coordinate frame to the world coordinate frame and from the end-effector coordinate frame to the joint 4 coordinate frame are:

$${}^wT_0 = \begin{bmatrix} 1 & 0 & 0 & 0 \\ 0 & 1 & 0 & 0 \\ 0 & 0 & 1 & \alpha_0 \\ 0 & 0 & 0 & 1 \end{bmatrix} \quad {}^4T_e = \begin{bmatrix} 1 & 0 & 0 & 0 \\ 0 & 1 & 0 & 0 \\ 0 & 0 & 1 & \alpha_g \\ 0 & 0 & 0 & 1 \end{bmatrix}$$



(a) impact coordinate frame (b) end-effector coordinate frame

Figure 2.3 Impact coordinate frame

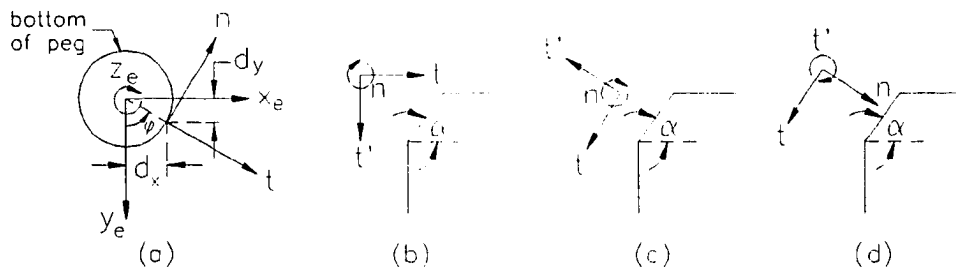


Figure 2.4 Transformation from impact coordinate frame to end-effector coordinate frame

The impact coordinate frame and end-effector coordinate frame are shown in Figure 2.3. The transformation steps from the impact coordinate frame to the end-effector coordinate frame are as follows (refer to Figure 2.4 and note that n - t - t' coincides with x_c - y_c - z_c finally):

1. Rotate an angle $-\varphi$ about the z_c axis, i.e., $R_{z_c, -\varphi}$ (Figure 2.4 (a))
2. Translate a distance d_x along the x_c axis, i.e., P_{x_c, d_x} (Figure 2.4 (a))
3. Translate a distance d_y along the y_c axis, i.e., P_{y_c, d_y} (Figure 2.4 (a))
4. Rotate an angle $180^\circ + \alpha$ about the n axis, i.e., $R_{n, 180^\circ + \alpha}$ (Figure 2.4 (c))
5. Rotate an angle 90° about the t axis, i.e., $R_{t, 90^\circ}$ (Figure 2.4 (d))

Figures 2.4 (a) and (b) are the top and side views after steps 1, 2, and 3.

Figures 2.4 (c) and (d) are the side views after steps 4 and 5, respectively.

The matrices associated with the above transformations are:

$$R_{z_c, -\varphi} = \begin{bmatrix} \cos -\varphi & -\sin -\varphi & 0 & 0 \\ \sin -\varphi & \cos -\varphi & 0 & 0 \\ 0 & 0 & 1 & 0 \\ 0 & 0 & 0 & 1 \end{bmatrix}$$

$$R_{n,180-\alpha} = \begin{bmatrix} 1 & 0 & 0 & 0 \\ 0 & \cos(180^\circ - \alpha) & -\sin(180^\circ - \alpha) & 0 \\ 0 & \sin(180^\circ - \alpha) & \cos(180^\circ - \alpha) & 0 \\ 0 & 0 & 0 & 1 \end{bmatrix}$$

$$R_{t,90} = \begin{bmatrix} \cos 90^\circ & 0 & \sin 90^\circ & 0 \\ 0 & 1 & 0 & 0 \\ -\sin 90^\circ & 0 & \cos 90^\circ & 0 \\ 0 & 0 & 0 & 1 \end{bmatrix} = \begin{bmatrix} 0 & 0 & 1 & 0 \\ 0 & 1 & 0 & 0 \\ -1 & 0 & 0 & 0 \\ 0 & 0 & 0 & 1 \end{bmatrix}$$

$$P_{x,d_x} = \begin{bmatrix} 1 & 0 & 0 & d_x \\ 0 & 1 & 0 & 0 \\ 0 & 0 & 1 & 0 \\ 0 & 0 & 0 & 1 \end{bmatrix}$$

$$P_{y,d_y} = \begin{bmatrix} 1 & 0 & 0 & 0 \\ 0 & 1 & 0 & d_y \\ 0 & 0 & 1 & 0 \\ 0 & 0 & 0 & 1 \end{bmatrix}$$

After the above transformation steps are performed, the final transformation matrix, which is the transformation matrix from the impact coordinate frame to the end-effector coordinate frame, is:

$${}^eT_p = P_{x,d_x} \cdot P_{y,d_y} \cdot R_{z,\varphi} \cdot R_{n,180-\alpha} \cdot R_{t,90}$$

$$= \begin{bmatrix} \sin \alpha \cos \varphi & -\cos \alpha \sin \varphi & \cos \varphi & d_x \\ \cos \varphi \sin \alpha & -\cos \alpha \sin \varphi & -\sin \varphi & d_y \\ \cos \alpha & \sin \alpha & 0 & 0 \\ 0 & 0 & 0 & 1 \end{bmatrix}$$

Link 1 and 2 have the shape of rectangular parallelepiped with two semi-cylindrical ends, but link 3 and 4 are cylinders. The pseudo inertia matrix of each link is as follows:

for link 1:

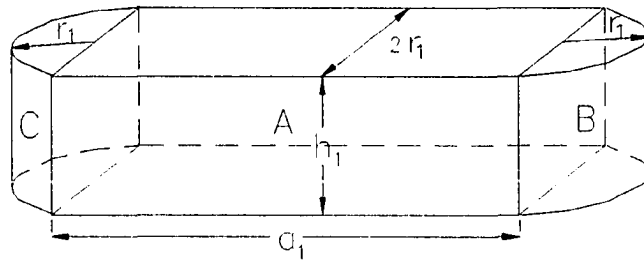


Figure 2.5 Shape and dimension of link 1

The shape and dimension of link 1 are shown in Figure 2.5. The inertia matrix of link 1 associated with the coordinate frame $x_1-y_1-z_1$ is:

$$\begin{bmatrix} J_{11}^1 & 0 & J_{13}^1 & J_{14}^1 \\ 0 & J_{22}^1 & 0 & 0 \\ J_{31}^1 & 0 & J_{33}^1 & J_{34}^1 \\ J_{41}^1 & 0 & J_{43}^1 & J_{44}^1 \end{bmatrix}$$

where:

$$J_{11}^1 = \frac{\alpha_1^2 m_{11}}{3} + \alpha_1^2 m_1^3 + \frac{8\alpha_1 m_{13} r_1}{3\pi} + \frac{m_{12} r_1^2}{4} + \frac{m_{13} r_1^2}{4}$$

$$J_{13}^1 = J_{31}^1 = \frac{d_1}{6\pi} (3\alpha_1 m_{11} \pi + 6\alpha_1 m_{13} \pi - 8m_{12} r_1 + 8m_{13} r_1)$$

$$J_{14}^1 = J_{41}^1 = -\frac{\alpha_1}{2} (m_{11} + m_{12} + m_{13})$$

$$J_{22}^1 = \frac{r_1^2}{12} (4m_{11} + 3m_{12} + 3m_{13})$$

$$J_{33}^1 = \frac{1}{12}(m_{11} + m_{12} + m_{13})(h_1^2 + 12d_1^2)$$

$$J_{34}^1 = J_{43}^1 = d_1(m_{11} + m_{12} + m_{13})$$

$$J_{44}^1 = (m_{11} + m_{12} + m_{13})$$

m_{11} : mass of part A in link 1

m_{12} : mass of part B in link 1

m_{13} : mass of part C in link 1

for link 2:

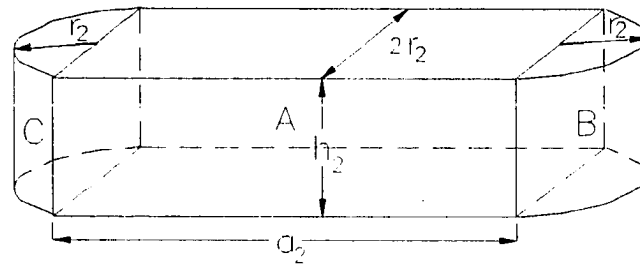


Figure 2.6 Shape and dimension of link 2

The shape and dimension of link 2 are shown in Figure 2.6. The inertia matrix of link 2 associated with the coordinate frame x_2 - y_2 - z_2 is:

$$\begin{bmatrix} J_{11}^2 & 0 & 0 & J_{14}^2 \\ 0 & J_{22}^2 & 0 & 0 \\ 0 & 0 & J_{33}^2 & 0 \\ J_{41}^2 & 0 & 0 & J_{44}^2 \end{bmatrix}$$

where:

$$J_{11}^2 = \frac{\alpha_1^2 m_{11}}{3} + \alpha_1^2 m_1^3 + \frac{8\alpha_1 m_{13} r_1}{3\pi} + \frac{m_{12} r_1^2}{4} + \frac{m_{13} r_1^2}{4}$$

$$J_{14}^2 = J_{41}^2 = -\frac{\alpha_2}{2}(m_{21} + m_{22} + m_{23})$$

$$J_{22}^2 = \frac{r_2^2}{12}(4m_{21} + 3m_{22} + 3m_{23})$$

$$J_{33}^2 = \frac{h_2^2}{12}(m_{21} + m_{22} + m_{23})$$

$$J_{44}^2 = (m_{21} + m_{22} + m_{23})$$

m_{21} : mass of part A in link 2

m_{22} : mass of part B in link 2

m_{23} : mass of part C in link 2

for link 3 and 4:

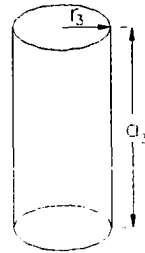


Figure 2.7 Shape and dimension of link 3 and 4

The shape and dimension of link 3 are shown in Figure 2.7. The inertia matrix of link 3 associated with the coordinate frame x_3 - y_3 - z_3 is

$$\begin{bmatrix} \frac{m_3 r_3^2}{4} & 0 & 0 & 0 \\ 0 & \frac{m_3 r_3^2}{4} & 0 & 0 \\ 0 & 0 & \frac{a_3^2 m_3}{3} & \frac{-a_3 m_3}{2} \\ 0 & 0 & \frac{-a_3 m_3}{2} & m_3 \end{bmatrix}$$

Link 3 and 4 are identical links, so link 4 has the same inertia matrix as the link 3.

Now, we can begin to derive the impact equations. We assume that the contact is a point contact, hence there is no angular momentum impulse. The derived impact equations using Equation (2.6) are

for joint 1:

$$\Delta\left(\frac{\partial K}{\partial \dot{q}_1}\right) = H_1 \Rightarrow$$

$$\begin{aligned} & \left[\frac{m_{11}a_1^2}{3} + \frac{m_{21}a_2^2}{3} + \frac{8a_1m_{13}r_1}{3\pi} + \frac{m_{11}r_1^2}{3} + \frac{m_{12}r_1^2}{2} + \frac{m_{13}r_1^2}{2} + \frac{m_{22}r_2^2}{2} + \frac{8a_2m_{23}r_2}{3\pi} \right. \\ & \quad + \frac{m_{21}r_2^2}{3} + m_{13}a_1^2 + m_{22}a_1^2 + m_{21}a_1^2 + 2m_3a_2^2 + m_{23}a_1^2 + m_{23}a_2^2 + 2m_3a_1^2 \\ & \quad + 2m_3a_2^2 + m_3r_3^2 + m_{21}a_1a_2 \cos \theta_2 + m_{22}a_1a_2 \cos \theta_2 + m_{23}a_1a_2 \cos \theta_2 \\ & \quad \left. + \frac{m_{23}r_2^2}{2} + 4m_3a_1a_2 \cos \theta_2 \right] (\dot{\theta}'_1 - \dot{\theta}_1) \\ & + \left[\frac{m_{21}a_2^2}{3} + \frac{m_{21}r_2^2}{3} + m_{23}a_2^2 + m_3a_2^2 + \frac{8m_{23}a_2r_2}{3\pi} + m_3r_3^2 + \frac{m_{22}r_2^2}{2} + \frac{m_{23}r_2^2}{2} \right. \\ & \quad \left. + \frac{1}{2}m_{21}a_1a_2 \cos \theta_2 + \frac{1}{2}m_{22}a_1a_2 \cos \theta_2 + 2m_3a_1a_2 \cos \theta_2 \right] \\ & \quad + \frac{1}{2}m_{23}a_1a_2 \cos \theta_2 \left] (\dot{\theta}'_2 - \dot{\theta}_2) \right. \\ & \quad \left. + \left[\frac{-m_3r_3^2}{2} \right] (\dot{\theta}'_4 - \dot{\theta}_4) \right. \\ & = a_1 \left[-\cos(\varphi - \theta_4 + \theta_2) \sin \alpha \right] P_n + a_1 \left[\cos(\varphi - \theta_4 + \theta_2) \cos \alpha \right] P_r \\ & \quad - a_1 \left[\cos(\varphi - \theta_4 + \theta_2) \right] P_t \end{aligned} \tag{2.7}$$

for joint 2:

$$\Delta\left(\frac{\partial K}{\partial \dot{q}_2}\right) = H_2 \Rightarrow$$

$$\begin{aligned}
& \left[\frac{m_{21}a_2^2}{3} + \frac{m_{21}r_2^2}{3} + m_{23}a_2^2 + m_3a_2^2 + \frac{8m_{23}a_2r_2}{3\pi} + m_3r_3^2 + \frac{m_{22}r_2^2}{2} + \frac{m_{23}r_2^2}{2} \right. \\
& \left. + \frac{1}{2}m_{21}a_1a_2 \cos \theta_2 + \frac{1}{2}m_{22}a_1a_2 \cos \theta_2 + \frac{1}{2}m_{23}a_1a_2 \cos \theta_2 + 2m_3a_1a_2 \cos \theta_2 \right] (\dot{\theta}'_1 - \dot{\theta}_1) \\
& + \left[\frac{m_{21}a_2^2}{3} + \frac{m_{21}r_2^2}{3} + m_{23}a_2^2 + m_3a_2^2 + \frac{8m_{23}a_2r_2}{3\pi} + m_3r_3^2 + \frac{m_{22}r_2^2}{2} + \frac{m_{23}r_2^2}{2} \right] (\dot{\theta}'_2 - \dot{\theta}_2) \\
& + \left[\frac{-m_3r_3^2}{2} \right] (\dot{\theta}'_4 - \dot{\theta}_4) \\
& = a_2 [-\cos(\varphi - \theta_4) \sin \alpha] P_n + a_2 [\cos(\varphi - \theta_4) \cos \alpha] P_t - a_2 [\cos(\varphi - \theta_4)] P_r
\end{aligned} \tag{2.8}$$

for joint 3:

$$\Delta \left(\frac{\partial K}{\partial \dot{q}_3} \right) = H_3 \Rightarrow$$

$$2m_3(\dot{d}'_3 - \dot{d}_3) = \cos \alpha \cdot P_n + \sin \alpha \cdot P_t \tag{2.9}$$

for joint 4:

$$\Delta \left(\frac{\partial K}{\partial \dot{q}_4} \right) = H_4 \Rightarrow$$

$$\begin{aligned}
& \left[\frac{-m_3r_3^2}{2} \right] (\dot{\theta}'_1 - \dot{\theta}_1) + \left[\frac{-m_3r_3^2}{2} \right] (\dot{\theta}'_2 - \dot{\theta}_2) + \left[\frac{-m_3r_3^2}{2} \right] (\dot{\theta}'_4 - \dot{\theta}_4) \\
& = [d_x \cos \varphi \sin \alpha - d_y \sin \varphi \sin \alpha] P_n - [-d_x \cos \varphi \cos \alpha + d_y \sin \varphi \cos \alpha] P_t \\
& \quad + [-d_x \sin \varphi - d_y \cos \varphi] P_r
\end{aligned} \tag{2.10}$$

In addition to the above four impact equations, three more equations are needed to solve for the seven unknowns: $\dot{\theta}'_1$, $\dot{\theta}'_2$, $\dot{\theta}'_3$, $\dot{\theta}'_4$, P_n , P_t , and P_c . These three equations can be obtained from the definitions of coefficients of restitution and coefficient of friction. The normal speed after impact is equal to the normal speed before impact multiplied by the coefficient of restitution, e . This relationship can be written in terms of the joint speeds before and after impact as follows:

$$\begin{aligned}
& \left\{ -\sin \alpha [a_1 \cos(\varphi + \theta_2 - \theta_4) + a_2 \cos(\varphi - \theta_4)] \right\} \dot{\theta}'_1 \\
& + \left\{ -a_2 \sin \alpha \cos(\varphi - \theta_4) \right\} \dot{\theta}'_2 \\
& + \left\{ \cos \alpha \right\} \dot{d}'_3 \\
= & -e \left\{ \left\{ -\sin \alpha [a_1 \cos(\varphi + \theta_2 - \theta_4) + a_2 \cos(\varphi - \theta_4)] \right\} \dot{\theta}'_1 \right. \\
& + \left\{ -a_2 \sin \alpha \cos(\varphi - \theta_4) \right\} \dot{\theta}'_2 \\
& \left. + \left\{ \cos \alpha \right\} \dot{d}'_3 \right\}
\end{aligned} \tag{2.11}$$

The tangential impulse P_t , P_c , and normal impulse are related by the coefficients of friction, μ , as

$$P_t = \mu P_n \tag{2.12}$$

$$P_c = \mu P_n \tag{2.13}$$

Equations (2.7) to (2.13) form the system's equations whose matrix is

$$\begin{bmatrix} a_{11} & a_{12} & 0 & a_{14} & a_{15} & a_{16} & a_{17} \\ a_{21} & a_{22} & 0 & a_{24} & a_{25} & a_{26} & a_{27} \\ 0 & 0 & a_{33} & 0 & a_{35} & a_{36} & 0 \\ a_{41} & a_{42} & 0 & a_{44} & a_{45} & a_{46} & a_{47} \\ a_{51} & a_{52} & a_{53} & 0 & 0 & 0 & 0 \\ 0 & 0 & 0 & 0 & \mu & -1 & 0 \\ 0 & 0 & 0 & 0 & \mu & 0 & -1 \end{bmatrix} \begin{bmatrix} \dot{\theta}'_1 \\ \dot{\theta}'_2 \\ \dot{d}'_3 \\ \dot{\theta}'_4 \\ P_n \\ P_t \\ P_r \end{bmatrix} = \begin{bmatrix} a_{11}\dot{\theta}_1 + a_{12}\dot{\theta}_2 + a_{14}\dot{\theta}_4 \\ a_{21}\dot{\theta}_1 + a_{22}\dot{\theta}_2 + a_{24}\dot{\theta}_4 \\ a_{33}\dot{d}_3 \\ a_{41}\dot{\theta}_1 + a_{42}\dot{\theta}_2 + a_{44}\dot{\theta}_4 \\ -e(a_{51}\dot{\theta}_1 + a_{52}\dot{\theta}_2 + a_{53}\dot{d}_3) \\ 0 \\ 0 \end{bmatrix} \quad (2.14)$$

where

$$\begin{aligned}
a_{11} = & \left[\frac{m_{11}a_1^2}{3} + \frac{m_{21}a_2^2}{3} + \frac{8a_1m_{13}r_1}{3\pi} + \frac{m_{11}r_1^2}{3} + \frac{m_{12}r_1^2}{2} + \frac{m_{13}r_1^2}{2} + \frac{m_{22}r_2^2}{2} + \frac{8a_2m_{23}r_2}{3\pi} \right. \\
& + \frac{m_{21}r_2^2}{3} + m_{13}a_1^2 + m_{22}a_1^2 + m_{21}a_1^2 + 2m_3a_2^2 + m_{23}a_1^2 + m_{23}a_2^2 + 2m_3a_1^2 \\
& + 2m_3a_2^2 + m_3r_3^2 + m_{21}a_1a_2 \cos \theta_2 + m_{22}a_1a_2 \cos \theta_2 + m_{23}a_1a_2 \cos \theta_2 \\
& \left. + \frac{m_{23}r_2^2}{2} + 4m_3a_1a_2 \cos \theta_2 \right]
\end{aligned}$$

$$\begin{aligned}
a_{12} = & \left[\frac{m_{21}a_2^2}{3} + \frac{m_{21}r_2^2}{3} + m_{23}a_2^2 + m_3a_2^2 + \frac{8m_{23}a_2r_2}{3\pi} + m_3r_3^2 + \frac{m_{22}r_2^2}{2} + \frac{m_{23}r_2^2}{2} \right. \\
& \left. + \frac{1}{2}m_{21}a_1a_2 \cos \theta_2 + \frac{1}{2}m_{22}a_1a_2 \cos \theta_2 + \frac{1}{2}m_{23}a_1a_2 \cos \theta_2 + 2m_3a_1a_2 \cos \theta_2 \right]
\end{aligned}$$

$$a_{14} = \left[\frac{-m_3r_3^2}{2} \right]$$

$$a_{15} = a_1 [\cos(\varphi - \theta_4 + \theta_2) \sin \alpha]$$

$$a_{16} = -a_1 [\cos(\varphi - \theta_4 + \theta_2) \cos \alpha]$$

$$a_{17} = a_1 [\sin(\varphi - \theta_4 + \theta_2)]$$

$$\alpha_{21} = \left[\frac{m_{21}a_2^2}{3} + \frac{m_{21}r_2^2}{3} + m_{23}a_2^2 + m_3a_2^2 + \frac{8m_{23}a_2r_2}{3\pi} + m_3r_3^2 + \frac{m_{22}r_2^2}{2} + \frac{m_{23}r_2^2}{2} + \frac{1}{2}m_{21}a_1a_2 \cos \theta_2 + \frac{1}{2}m_{22}a_1a_2 \cos \theta_2 + \frac{1}{2}m_{23}a_1a_2 \cos \theta_2 + 2m_3a_1a_2 \cos \theta_2 \right]$$

$$\alpha_{22} = \left[\frac{m_{21}a_2^2}{3} + \frac{m_{21}r_2^2}{3} + m_{23}a_2^2 + m_3a_2^2 + \frac{8m_{23}a_2r_2}{3\pi} + m_3r_3^2 + \frac{m_{22}r_2^2}{2} + \frac{m_{23}r_2^2}{2} \right]$$

$$\alpha_{24} = \left[\frac{-m_3r_3^2}{2} \right]$$

$$\alpha_{25} = a_2 [\cos(\varphi - \theta_4) \sin \alpha]$$

$$\alpha_{26} = -a_2 [\cos(\varphi - \theta_4) \cos \alpha]$$

$$\alpha_{27} = a_2 [\sin(\varphi - \theta_4)]$$

$$\alpha_{33} = -2m_3$$

$$\alpha_{35} = \cos \alpha$$

$$\alpha_{36} = \sin \alpha$$

$$\alpha_{41} = \left[\frac{-m_3r_3^2}{2} \right]$$

$$\alpha_{42} = \left[\frac{-m_3r_3^2}{2} \right]$$

$$\alpha_{44} = \left[\frac{m_3r_3^2}{2} \right]$$

$$\alpha_{45} = -[d_x \cos \varphi \sin \alpha - d_y \sin \varphi \sin \alpha]$$

$$\alpha_{46} = [-d_x \cos \varphi \cos \alpha + d_y \sin \varphi \cos \alpha]$$

$$\alpha_{47} = -[-d_x \sin \varphi - d_y \cos \varphi]$$

$$\alpha_{51} = -\sin \alpha [a_1 \cos(\varphi + \theta_2 - \theta_4) + a_2 \cos(\varphi - \theta_4)]$$

$$a_{52} = -a_2 \sin \alpha \cos(\varphi - \theta_4)$$

$$a_{53} = \cos \alpha$$

One can easily obtain the joint velocities and components of the impulse after impact from the above system's equations.

2.5 Effect of Parameters on Impulse and Departure Angle

We investigate in this section how the impulse and departure angle in the peg-in-hole assembly depend upon robot configuration, link mass, link length, insertion speed, chamfer angle and coefficient of restitution for the SCARA-type robot described in section 2.4. The departure angle is defined as the angle between the tip velocity of the peg at the end of impact and the chamfer surface as shown in Figure 2.8. The departure angle depicts the part motion after colliding. Both the impulse and the departure angle are desired to be as small as possible for successful parts mating.

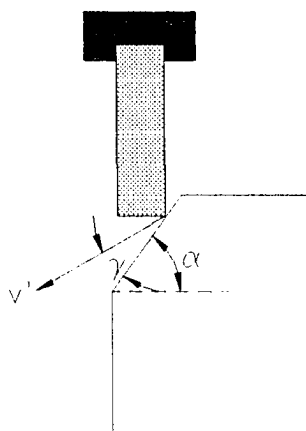


Figure 2.8 The departure angle and chamfer angle

Since the system's equations are very complex, only part of parameters can be analytically investigated. For those parameters which are difficult to be analytically investigated, numerical simulation will be used. From the third row and the last two rows of Equation (2.14), the normal impulse P_n is:

$$P_n = \frac{2m_3(\dot{d}'_3 - \dot{d}_3)}{\cos \alpha + \mu \sin \alpha} \quad (2.15)$$

The velocity changes of joints 1 and 2 can be obtained from the first row, second row, and fourth row of Equation (2.14) as follows:

$$\dot{\theta}'_1 - \dot{\theta}_1 = \frac{2m_3(\dot{d}'_3 - \dot{d}_3) N_1}{\cos \alpha + \mu \sin \alpha D} \quad (2.16)$$

$$\dot{\theta}'_2 - \dot{\theta}_2 = \frac{-2m_3(\dot{d}'_3 - \dot{d}_3) N_2}{\cos \alpha + \mu \sin \alpha D} \quad (2.17)$$

We then substitute (2.16) and (2.17) into the fifth row of Equation (2.14) and solve the resulting equation. The velocity change of joint 3 can be obtained as

$$\dot{d}'_3 - \dot{d}_3 = \frac{-D(1+e)(a_{51}\dot{\theta}_1 + a_{52}\dot{\theta}_2 + a_{53}\dot{d}_3)(\cos \alpha + \mu \sin \alpha)}{[2m_3(a_{51}N_1 - a_{52}N_2) + a_{53}D(\cos \alpha + \mu \sin \alpha)]} \quad (2.18)$$

Plugging (2.18) into (2.15) leads to

$$P_n = \frac{-2m_3 D(1+e)(\alpha_{51}\dot{\theta}_1 + \alpha_{52}\dot{\theta}_2 + \alpha_{53}\dot{d}_3)}{[2m_3(\alpha_{51}N_1 - \alpha_{52}N_2) + \alpha_{53}D(\cos\alpha + \mu\sin\alpha)]} \quad (2.19)$$

To analyze the departure angle, we need to find the velocity normal to the chamfer surface and the velocity on the chamfer surface. The normal velocity of the peg's tip after impact is

$$\begin{aligned} v'_n = & -a_2 \left(\dot{\theta}_2 + \frac{2m_3(\dot{d}'_3 - \dot{d}_3) N_2}{\cos\alpha + \mu\sin\alpha D} \right) \sin\theta_4 \\ & + \left(\dot{\theta}_1 - \frac{2m_3(\dot{d}'_3 - \dot{d}_3) N_1}{\cos\alpha + \mu\sin\alpha D} \right) [a_1 \sin(\theta_2 - \theta_4) - a_2 \sin\theta_4] \end{aligned} \quad (2.20)$$

and the tangential velocity after impact is

$$\begin{aligned} v'_t = & -a_2 \left(\dot{\theta}_2 + \frac{2m_3(\dot{d}'_3 - \dot{d}_3) N_2}{\cos\alpha + \mu\sin\alpha D} \right) \cos\theta_4 \\ & + \left(\dot{\theta}_1 - \frac{2m_3(\dot{d}'_3 - \dot{d}_3) N_1}{\cos\alpha + \mu\sin\alpha D} \right) [a_1 \cos(\theta_2 - \theta_4) - a_2 \cos\theta_4] \end{aligned} \quad (2.21)$$

The departure angle is

$$\gamma = \tan^{-1} \left(\frac{-v'_n}{v'_t} \right) \quad (2.22)$$

where

$$\begin{aligned} N_1 = & a_{14}a_{15} + a_{15}a_{22} - a_{12}a_{25} - a_{14}a_{25} - a_{12}a_{45} + a_{22}a_{45} + \mu a_{14}a_{16} + \mu a_{16}a_{22} \\ & - \mu a_{12}a_{26} - \mu a_{14}a_{26} - \mu a_{12}a_{46} + \mu a_{22}a_{46} + \mu' a_{14}a_{17} + \mu' a_{17}a_{22} \\ & - \mu' a_{12}a_{27} - \mu' a_{14}a_{27} - \mu' a_{12}a_{47} + \mu' a_{22}a_{47} \end{aligned}$$

$$\begin{aligned} N_2 = & a_{12}a_{15} + a_{14}a_{15} - a_{11}a_{25} - a_{14}a_{25} - a_{11}a_{45} + a_{12}a_{45} + \mu a_{12}a_{16} + \mu a_{14}a_{16} \\ & - \mu a_{11}a_{26} - \mu a_{14}a_{26} - \mu a_{11}a_{46} + \mu a_{12}a_{46} + \mu' a_{12}a_{17} + \mu' a_{14}a_{17} \\ & - \mu' a_{11}a_{27} - \mu' a_{14}a_{27} - \mu' a_{11}a_{47} + \mu' a_{12}a_{47} \end{aligned}$$

$$D = a_{12}^2 - a_{11}a_{14} + 2a_{12}a_{14} - a_{11}a_{22} - a_{14}a_{22}$$

Equations (2.19) and (2.22) do not include θ_1 , d_3 , and $\dot{\theta}_4$. Therefore, the angle of joint 1, the displacement of joint 3, and the velocity of joint 4 do not have any effect on either the normal impulse or the departure angle. However, the coefficient of restitution and the velocities of joint 1, 2, and 3 all have linear effect on the normal impulse.

Before numerical analysis, we would like to investigate the basic qualitative feature of functional dependence of normal impulse and departure angle. First, Equation (2.19) can be rewritten in the form

$$P_n = \frac{C_1 \sin \alpha + C_2 \cos \alpha}{\cos^2 \alpha + (\mu \cos \alpha + C_3 \mu + C_4) \sin \alpha} \quad (2.23)$$

where C_1 , C_2 , C_3 , and C_4 are functions depending only on e , φ , θ_2 , θ_4 , $\dot{\theta}_1$, $\dot{\theta}_2$, $\dot{\theta}_3$, and the robot geometry and masses. Thus, for example, if C_4 is much larger

than $1+|C_3|$, then P_n is nearly independent of the coefficient of friction μ . We also note that for any range of specification of the robot geometry, configuration and kinematics for which the signs of C_1 , C_2 , C_3 , and C_4 remain the same and $|C_4| \gg 1+|C_3|$, the basic qualitative feature of the functional dependence of P_n on the key variables such as α and μ remains the same. Hence, the numerical analysis of the functional properties of P_n for the particular choice of robot parameters that follows is essentially typical. A similar analysis of the equation for the departure angle γ leads to an analogous conclusion, namely, the functional properties obtained from numerical analysis of the equation represents typical behavior (at least within a fairly broad range of robot parameters).

In the numerical simulation described below, e equals to 0.3 and μ equal to 0.2 (unless differences are mentioned), and the robot parameters have the following nominal values (upon which variations are made):

Table 2.2 Nominal values of link parameters of a SCARA-type robot

$a_1 = 0.5 \text{ m}$	$a_2 = 0.4 \text{ m}$	$a_3 = 0.5 \text{ m}$	$a_4 = a_3$
$r_1 = 0.1 \text{ m}$	$r_2 = 0.08 \text{ m}$	$r_3 = 0.04 \text{ m}$	$r_4 = r_3$
$d_1 = 0.5 \text{ m}$	$d_2 = 0 \text{ m}$	$d_3 = 0.2 \text{ m}$	$d_4 = d_3$
$m_{11} = 20 \text{ kg}$	$m_{21} = 15 \text{ kg}$	$m_3 = 5 \text{ kg}$	$m_4 = m_3$
$m_{12} = 3 \text{ kg}$	$m_{13} = 3 \text{ kg}$	$m_{22} = 1 \text{ kg}$	$m_{23} = 1 \text{ kg}$

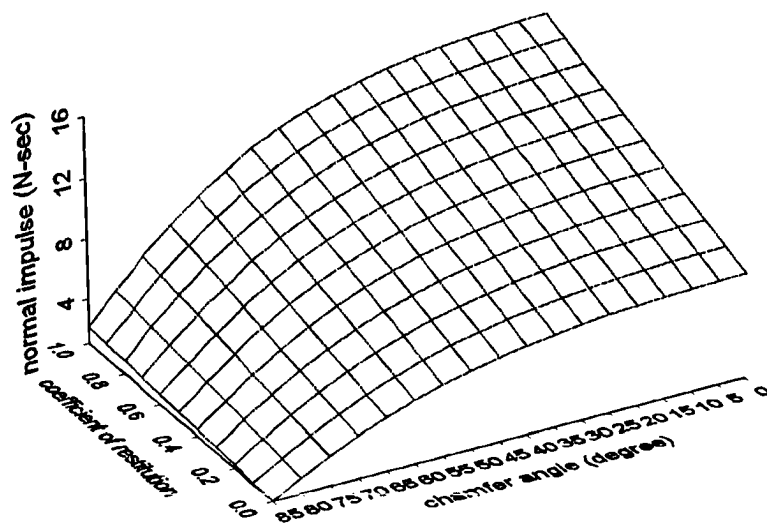


Figure 2.9 Normal impulse vs. coefficient of restitution and chamfer angle

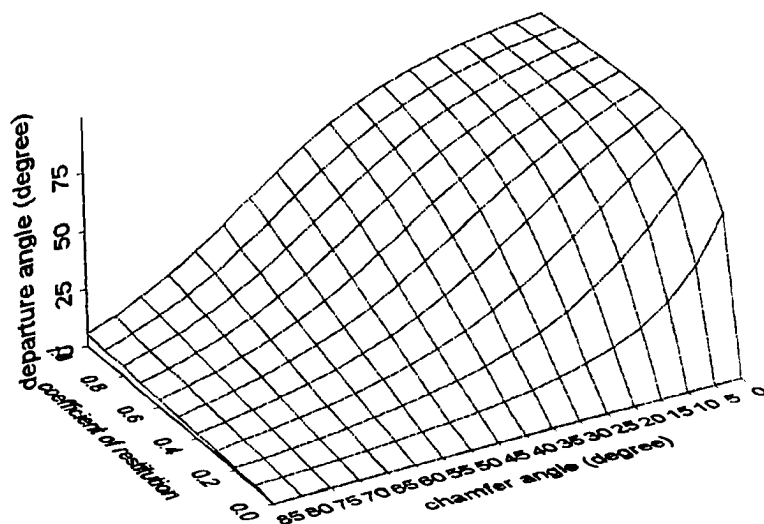


Figure 2.10 Departure angle vs. coefficient of restitution and chamfer angle

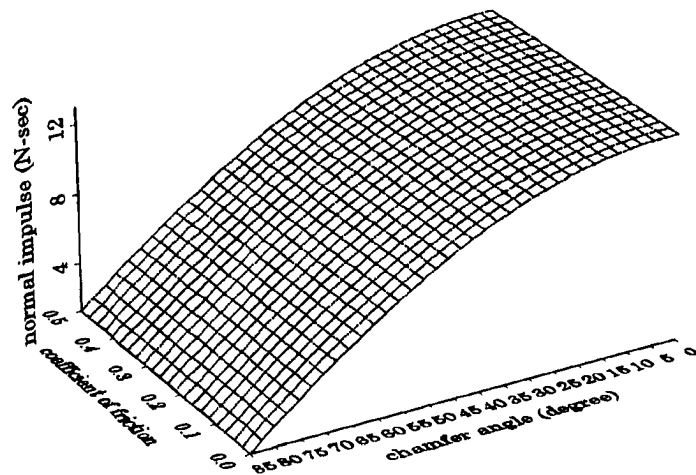


Figure 2.11 Normal impulse vs. coefficient of friction and chamfer angle

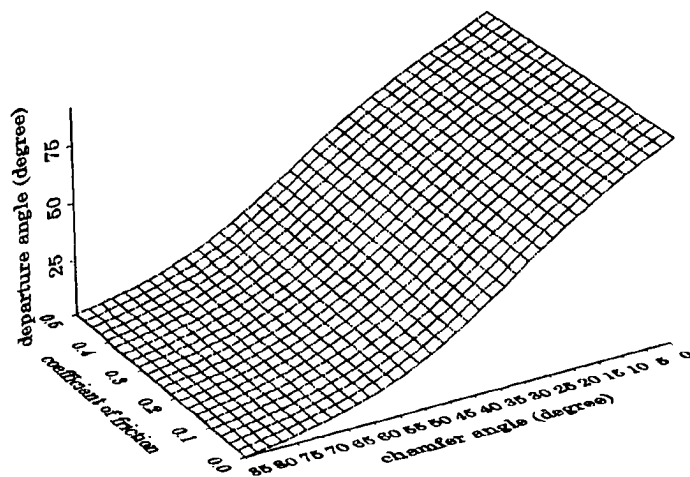


Figure 2.12 Departure angle vs. coefficient of friction and chamfer angle

Figure 2.9 plots normal impulse against coefficient of restitution and chamfer angle. The figure shows that a higher coefficient of restitution and a

smaller chamfer angle result in a larger impulse. The relationship between normal impulse and coefficient of restitution is linear. This can be seen from Equation (2.19). However, the normal impulse has a larger variation for change in chamfer angle when the chamfer angle is near 90° . The effect of the coefficient of restitution and chamfer angle on the departure angle is shown in Figure 2.10. The smaller the coefficient of restitution, the smaller the departure angle. This is due to the fact that a higher coefficient of restitution leads to a higher normal velocity after impact, which causes the direction of the rebound velocity further away from the chamfer surface. In the higher range of chamfer angle, the coefficient of restitution has a linear effect on the departure angle. However, the departure angle has significant variation in the lower range of chamfer angle when the coefficient of restitution is very small.

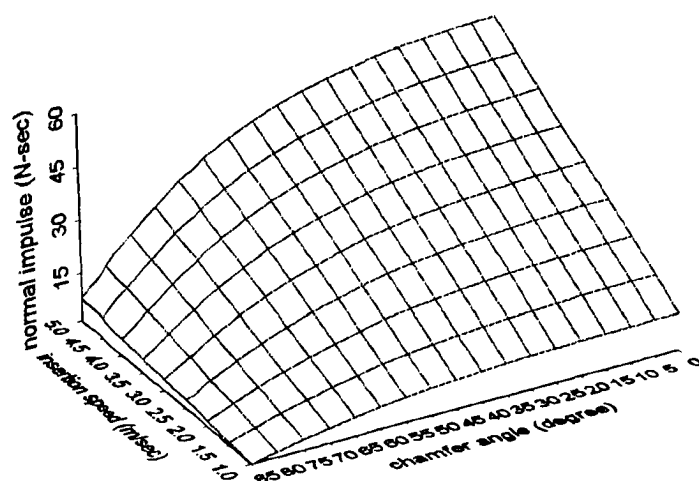


Figure 2.13 Normal impulse vs. insertion speed and chamfer angle

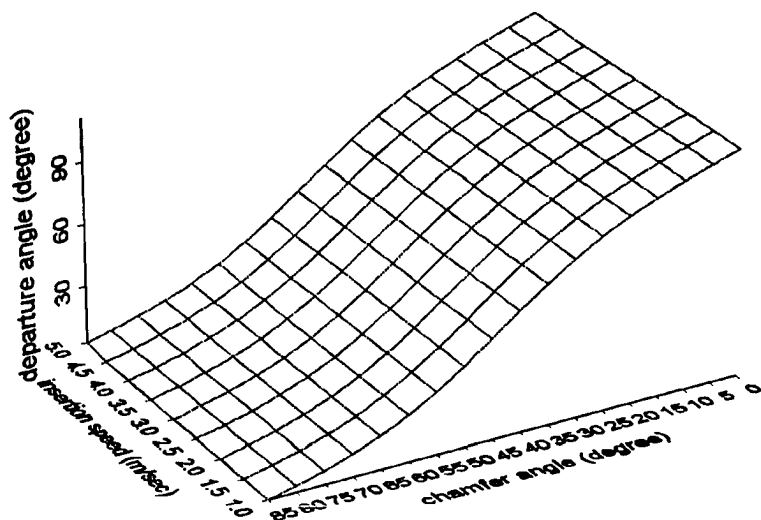


Figure 2.14 Departure angle vs. insertion speed and chamfer angle

Figures 2.11 and 2.12 show that the coefficient of friction does not affect the normal impulse and departure angle at all. The effects of insertion speed on normal impulse and departure angle are depicted in Figures 2.13 and 2.14, respectively. The normal impulse depends linearly on insertion speed. This can be verified from Equation (2.22) where the velocity of joint 3 has a linear effect on the normal impulse. However, the departure angle is independent of insertion speed.

Figures 2.15 to 2.20 show the effect of robot configuration on normal impulse and departure angle. These figures show that the normal impulse and departure angle have the same curve shapes versus variation in robot configurations and that joints 1 and 3 do not affect normal impulse and

departure angle. Figures 2.19 and 2.20 show that joints 2 and 4 are coupled in their effect on the normal impulse and departure angle.

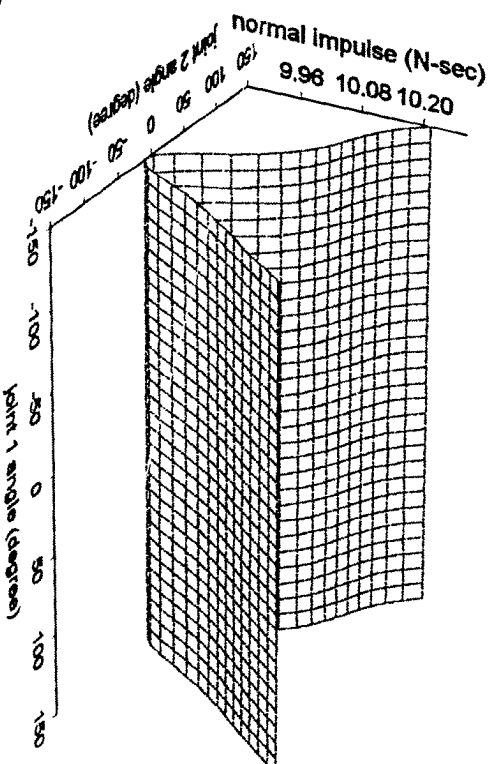


Figure 2.15 Normal impulse vs. joint 1 and joint 2 angles

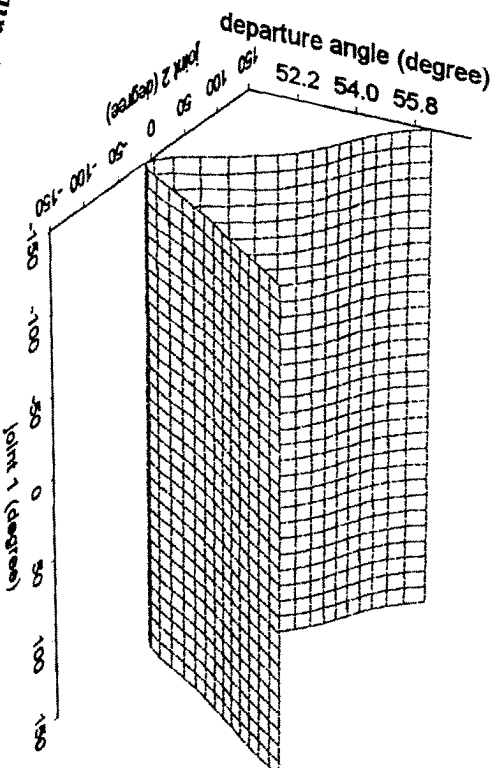


Figure 2.16 Departure angle vs. joint 1 and joint 2 angles

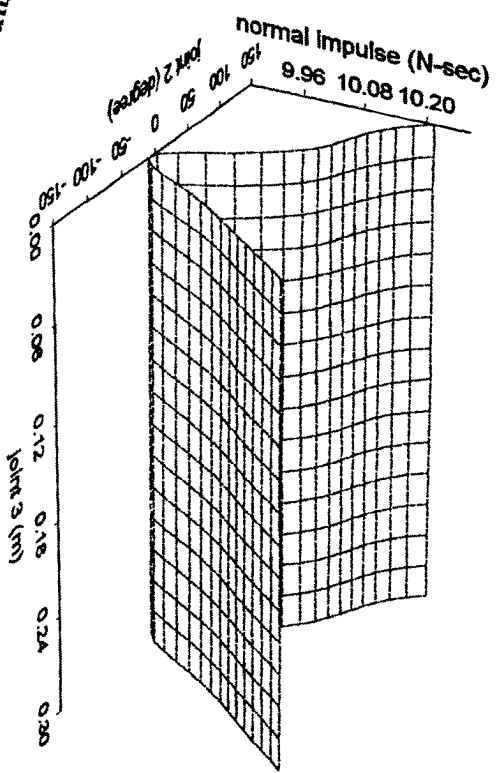


Figure 2.17 Normal impulse vs. joint 2 and joint 3 angles

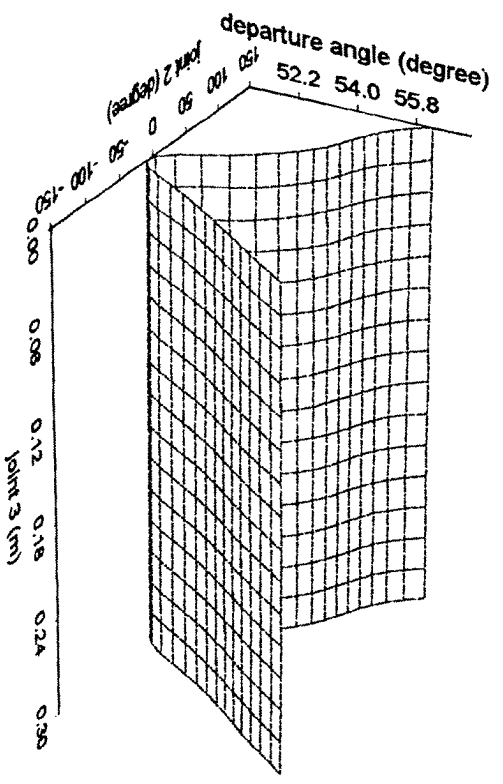


Figure 2.18 Departure angle vs. joint 2 and joint 3 angles

Reproduced with permission of the copyright owner. Further reproduction prohibited without permission.

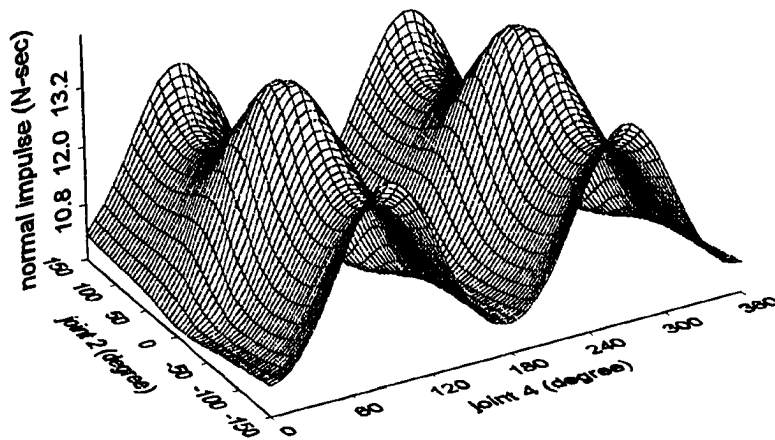


Figure 2.19 Normal impulse vs. joint 2 and joint 4 angles

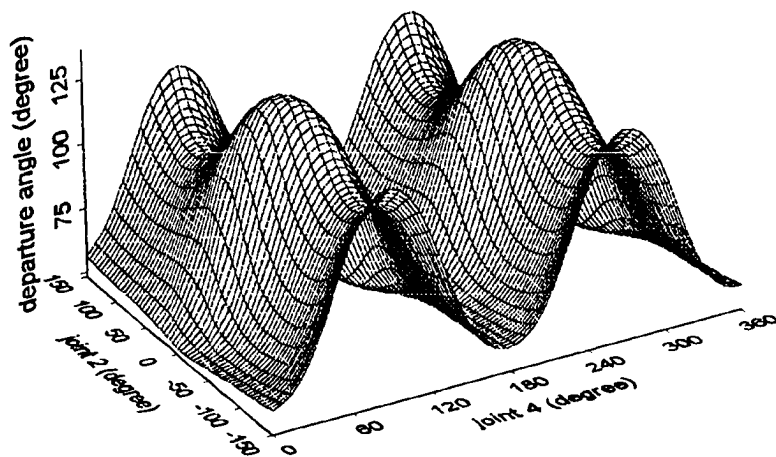


Figure 2.20 Departure angle vs. joint 2 and joint 4 angles

The effects of mass and length of links 1 and 2 are shown in Figures 2.21 to 2.24. The smaller the mass or length of link 1 or 2, the smaller the normal impulse and departure angle. The length of link 3 does not affect normal impulse and departure angle as seen from Equations (2.19) and (2.22). We analyze the effects of the radius and mass of link 3 in Figures (2.25) and (2.26). The normal impulse depends linearly on the mass of link 3; the larger the mass, the larger the normal impulse. However, the larger the mass, the smaller the departure angle. These figures also show that the radius of link 3 does not have any effect on the normal impulse and departure angle.

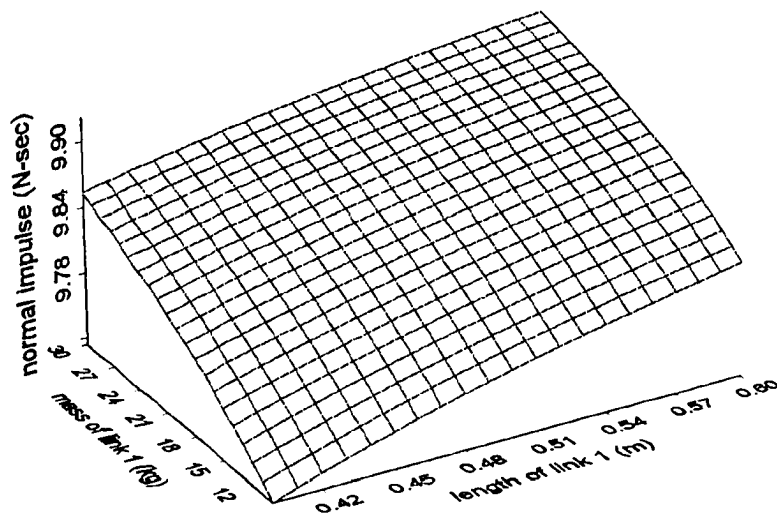


Figure 2.21 Normal impulse vs. mass and length of link 1

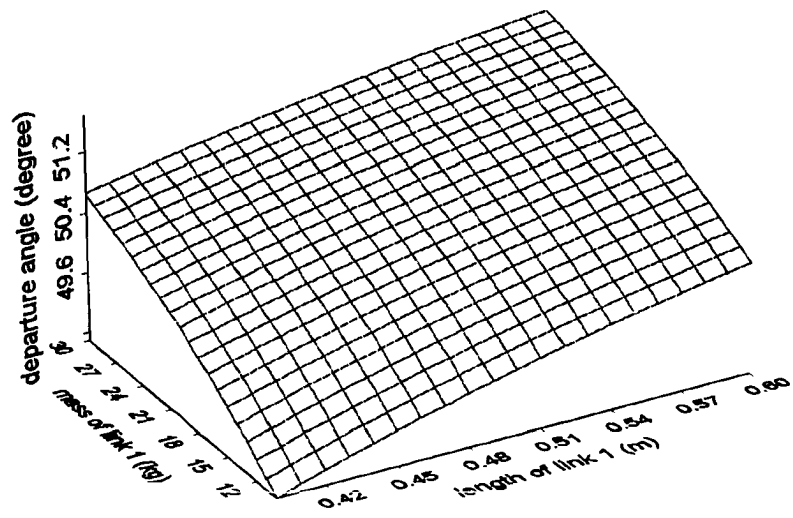


Figure 2.22 Departure angle vs. mass and length of link 1

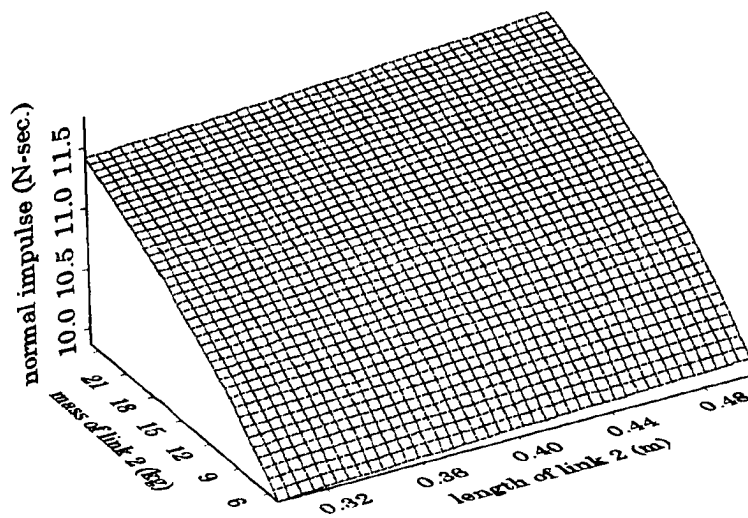


Figure 2.23 Normal impulse vs. mass and length of link 2

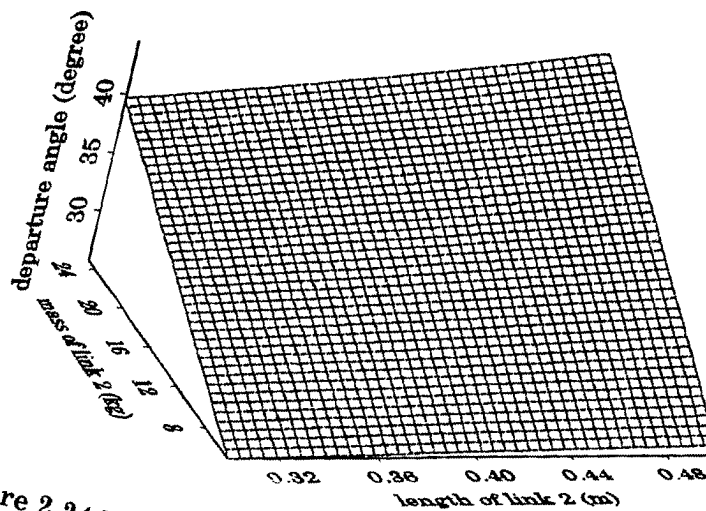


Figure 2.24 Departure angle vs. mass and length of link 2

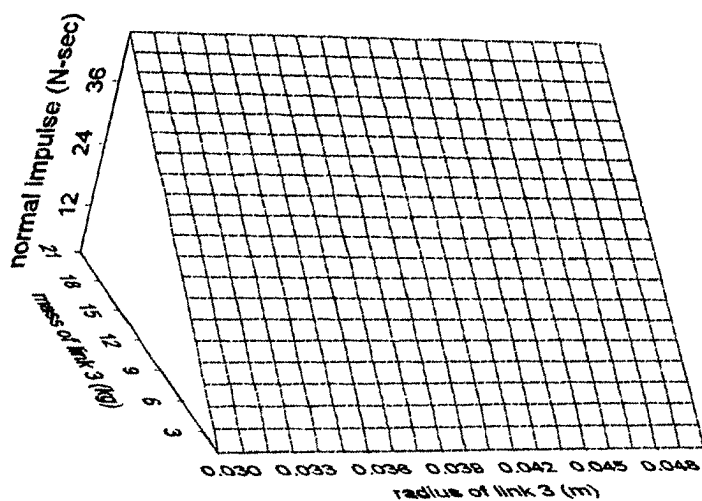


Figure 2.25 Normal impulse vs. mass and radius of link 3

Reproduced with permission of the copyright owner. Further reproduction prohibited without permission.

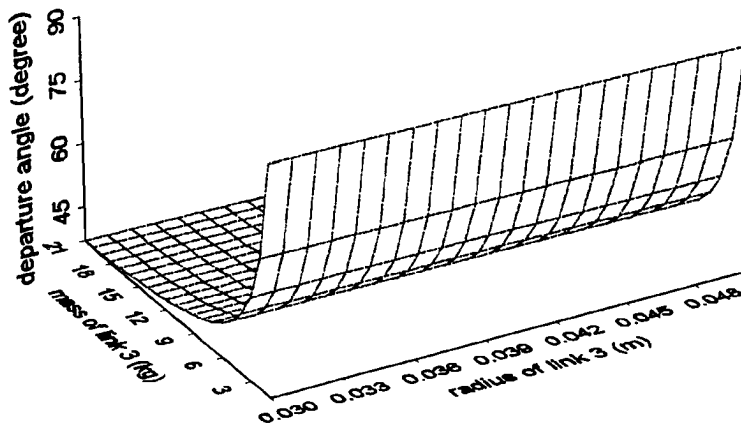


Figure 2.26 Departure angle vs. mass and radius of link 3

The above analytical and numerical results describe the dependence relations of normal impulse and departure angle on various parameters of the assembly system. This is useful to manipulator design and equipment layout planning in robotic assembly involving mating of parts. The goal of design and planning should be to minimize the impulsive force and departure angle, because a larger impulse may cause part damage and a larger departure angle is likely to cause assembly failure.

CHAPTER 3

EFFECT OF VIBRATION PARAMETERS ON ENGAGEMENT TIME

3.1 Introduction

Two kinds of vibration motion can increase tolerance to provide positional adjustment: increasing-amplitude vibration and constant-amplitude vibration. A circular spiral path, as shown in Figure 3.1 whose amplitude increases with time is an example of increasing-amplitude vibration. A study of increasing-amplitude vibration was presented by Leu and Katz (1994). Illustrated in Figure 3.2 is a constant-amplitude vibration whose sweep path is generated by two sinusoidal motions.

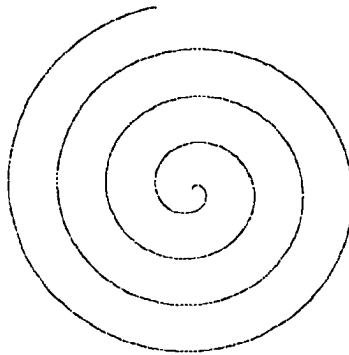


Figure 3.1 Increasing-amplitude vibration

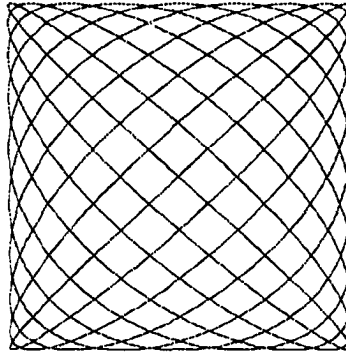


Figure 3.2 Constant-amplitude vibration

We will discuss here how to determine the optimal parameters of vibration for constant-amplitude vibration. It is a more complex problem to determine the optimal vibration parameters for constant-amplitude vibration than for increasing-amplitude vibration. One interesting and practical way of generating a sweep path is by applying sinusoidal motions. Sinusoidal motions are infinitely differentiable and they are relatively easy to generate mechanically. The sinusoidal motion is a typical kind of constant-amplitude vibration. In the case of mating two axisymmetric parts, the motion used to aid the engagement of the two parts can be generated by the combination of two translational, sinusoidal motions, i.e.

$$\begin{aligned} x &= A\sin(\omega t) \\ y &= B\sin(k\omega t + \theta) \end{aligned} \tag{3.1}$$

where A and B are the vibration amplitudes, ω is the radial frequency in the x direction, k is the ratio of the two frequencies, and θ is the phase angle.

3.2 Positional Uncertainty and Tolerance

Successful mating of parts requires that the task's total positional uncertainty be within the tolerance of the task for positional errors. Let us consider positional uncertainty and tolerance in assembly. Positional uncertainty always exists in assembly equipment. It might be caused by manufacturing errors, control errors, thermal effects, etc. Tolerance is related primarily to the geometry of the parts at the mating interface, and it represents the capability of the assembly to tolerate positional errors..

Let the uncertainty and tolerance of an assembly be denoted by sets U and T , respectively. In the mating of two parts, positional uncertainty generally exists in both parts. Pai & Leu (1991) presented a study of task uncertainty and tolerance and their effects on assembly task feasibility. They considered the uncertainty of a task performed by a robot to consist of an end-effector uncertainty set U_1 and a task uncertainty set U_2 : The total uncertainty is then $U = U_1 \ominus U_2$, where \ominus is a mathematical symbol for set difference.

Two possible relations between uncertainty U and tolerance T in an assembly task are illustrated in Figure 3.3, which depicts that T may contain

U (i.e. $T \supset U$) or T may be contained by U (i.e. $T \subset U$). Clearly, engagement between two parts succeeds if $T \supset U$ but fails if $T \subset U$.

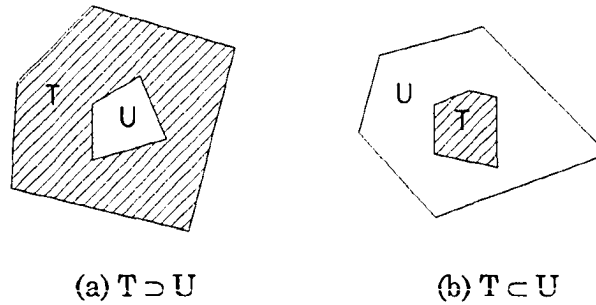


Figure 3.3 Two possible relations between uncertainty set U and tolerance set T

The principle of vibration-assisted mating of parts is to apply vibration to one of two mating parts such that the relative movement between the parts follows a planned sweep path S satisfying

$$\int_S T ds \supset U \quad (3.2)$$

Essentially, the introduction of the relative movement has enhanced the tolerance capacity of the assembly system for positional uncertainty in the assembly equipment.

3.3 Vibration Amplitude

Figure 3.4 shows key parameters of the uncertainty and tolerance sets in planar assembly. T_1 is the original tolerance set, and T_2 is a rectangular box within the T_1 set, i.e. $T_2 \subset T_1$. T_2 is used to avoid any U region not covered by the sweet of T_1 . In the round peg-in-hole insertion, T_1 is usually a circle. The point C_t is the center of T_2 . The distances from the center of the T_2 to the boundary of the uncertainty in x and y directions are $U_x^1, U_x^2, U_y^1,$ and U_y^2 as shown in the figure.

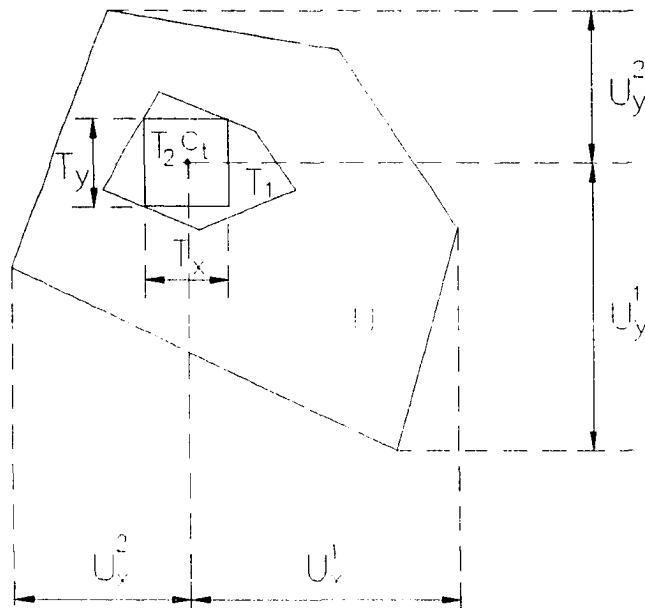


Figure 3.4 Sizes of uncertainty set U and tolerance set T

For feasible parts mating, the amplitudes A and B of the two applied sinusoidal motions must satisfy

$$\begin{aligned}
 A &\geq \max\left(U_x^1 - \frac{T_x}{2}, U_x^2 - \frac{T_x}{2}\right) \\
 B &\geq \max\left(U_y^1 - \frac{T_y}{2}, U_y^2 - \frac{T_y}{2}\right)
 \end{aligned}
 \tag{3.3}$$

The equal sign is used for minimizing the engagement time and reducing the insertion force. We will discuss this relationship later. In practice, since the relative motion between mating parts can not stop immediately after the peg lies within the tolerance area, a safety factor should be used to ensure successful engagement.

3.4 Vibration Frequency

Since the vibration frequency affects the speed of motion but not the sweep path, the vibration frequency should be as high as possible. However, in practice, this frequency must be limited so as to reduce changes in position during the response delay caused by the communication time between assembly assisted devices and the time to execute the “stop motion” command. A large movement during the delay may result in engagement failure. The consideration of selecting vibration frequency is as follows:

The derivative of Equation (3.1) is

$$\begin{aligned}
 x' &= \omega A \cos(\omega t) \\
 y' &= k\omega B \cos(k\omega t + \theta)
 \end{aligned}
 \tag{3.4}$$

Hence, the maximum lateral speed is

$$v_l = \omega \sqrt{A^2 + (kB)^2} \quad (3.5)$$

Suppose t_d is the communication delay time. We now consider mating of a round peg with a round hole. To avoid the peg moving out of the engagement region due to the delay time, it is required that

$$v_l t_d \leq 2(w + cR) \quad (3.6)$$

where c is the clearance ratio which is equal to $(R - r_g) / R$, R is the radius of the hole and r_g is the radius of the peg. By substituting (3.5) into (3.6), the vibration frequency ω should satisfy

$$\omega \leq \frac{2(w + cR)}{t_d \sqrt{A^2 + (kB)^2}} \quad (3.7)$$

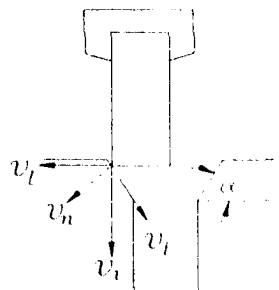


Figure 3.5 Sliding motion on chamfer surface

Another consideration is the relative velocity between the peg and the chamfer when the peg first contacts the chamfer after the search motion. When the peg begins to contact with the chamfer surface, the motion of the peg relative to the hole can be decomposed to two components: v_t which is parallel to the chamfer surface and v_n which is perpendicular to the chamfer surface as shown in Figure 3.5. The insertion may fail if

$$v_t = v_i \sin \alpha - v_n \cos \alpha < 0 \quad (3.8)$$

because the satisfaction of this equation results in a peg escaping motion, i.e., the peg slides upward away from the hole instead of downward into the hole. Hence, the vibration frequency ω should satisfy

$$\omega < \frac{v_i \tan \alpha}{\sqrt{A^2 + (kB)^2}} \quad (3.9)$$

The third consideration is avoidance of resonance of the assembly system. Suppose ω_n is the first nature frequency of the assembly system. To avoid the system resonance, the vibration frequency ω should satisfy

$$\omega < \frac{\omega_n}{2} \quad (3.10)$$

Therefore, the final selection of the vibration frequency should be

$$\omega = \min \left\{ \frac{2(w+cR)}{t_d \sqrt{A^2 + (kB)^2}}, \frac{v_i \tan \alpha}{\sqrt{A^2 + (kB)^2}}, \frac{\omega_n}{2} \right\} \quad (3.11)$$

3.5 Algorithm for Determining Required Sweep Time

To determine the optimal path produced by sinusoidal motions in two orthogonal directions, the frequency ratio k and phase angle θ of the two vibration motions also need to be considered. It is difficult to analytically find the optimal frequency ratio k and phase angle θ for a given uncertainty set U and tolerance set T . A possible approach is to numerically determine the optimal value of k and phase angle θ where equation (3.2) can be satisfied in the shortest time. Figure 3.6 illustrates the numerical approach for determining the minimum time to sweep the whole uncertainty area for given vibration parameters. The rectangle of dimensions $2A$ and $2B$ (A and B are obtained from Equation 3.3) is divided into many smaller rectangles whose widths are T_x and heights are $2B$, except for the two boundary rectangles whose widths are equal to or smaller than T_x . The horizontal coordinates of these lines and two boundary lines are denoted as x_i , $i=0,1,2,\dots,n$ where $n = \text{integer}[2A/T_x] + 2$ if $[2A/T_x]$ is not an integer or $n = \text{integer}[2A/T_x] + 1$ if $[2A/T_x]$ is an integer. Suppose that after some time, the

sweep path intersects x_i at point $y_{i,j}$, $j=1,2,\dots,m$ where m is the number of intersection points of the sweep path and the line segment $x = x_i$. Also, let $y_{i,0}$ and $y_{i,m+1}$ be the two y boundary values the y at $x=x_i$. Equation (3.2) is satisfied if $y_{i,j+1} - y_{i,j} \leq T_y$ for every $i \in \{0,1,2,\dots,n\}$ and $j \in \{0,1,2,\dots,m\}$. Then the required time of motion for the sweep of the tolerance region to cover the whole uncertainty region can be obtained numerically as will be described in an algorithm. By iteratively changing k and θ and computing the corresponding time of motion needed for successful engagement, the optimal frequency ratio and phase angle can be determined.

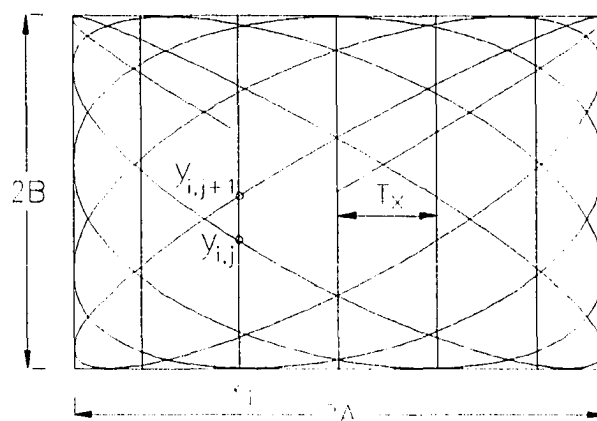


Figure 3.6 Sweep path for helping engagement

The algorithm for determining the sweep time required for engagement of parts for a specified frequency and phase angle is as follows:

1. The rectangle of dimensions $2A$ and $2B$ is divided into many smaller rectangles whose widths are T_x and heights are $2B$, except for the two boundary rectangles whose widths are equal to or smaller than T_x .
2. Determine the horizontal coordinates of the two boundary lines and the lines that divide $2A$. Denote these coordinates as x_i , $i=0,1,2,\dots,n$ where $n = \text{integer}[2A/T_x] + 2$ if $[2A/T_x]$ is not an integer or $n = \text{integer}[2A/T_x] + 1$ if $[2A/T_x]$ is an integer.
3. For each x_i , compute the y coordinates for the intersecting points between the sweep path and $x = x_i$, $i = 0,1,2,\dots,n$.
4. Sort all y coordinates such that $y_{i,j+1} > y_{i,j}$, $j = 1, 2, \dots, m$ and let $y_{i,0} = y_{\min}(x = x_i)$, $y_{i,m+1} = y_{\max}(x = x_i)$ for each $x = x_i$.
5. Compute $y_{i,j+1} - y_{i,j}$, $j = 0,1,2,\dots,m$ for each $x = x_i$. If all the distances $\{y_{i,j+1} - y_{i,j}\} \leq T_y$, $i = 0, 1, 2, \dots, n$, $j = 0,1,2,\dots,m$, record t , i.e., the required sweep time, otherwise continue to the next intersecting point where $t \Rightarrow t + \Delta t$, and go back to step 3.

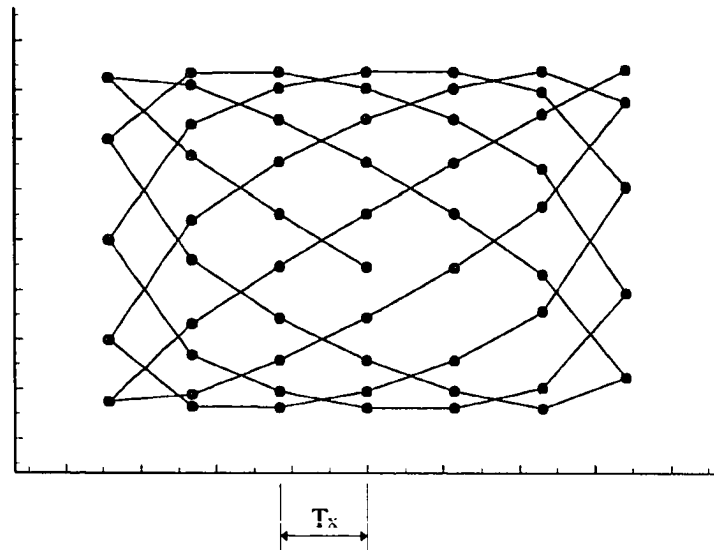


Figure 3.7 Sampling point of sweep path

The symbol • in Figure 3.7 is the intersecting point of the sweep path and a vertical line. Once all of the distances between two consecutive points in each vertical line are smaller or equal to T_y , the time is the required sweep time for successful engagement.

3.6 Numerical Results and Discussion

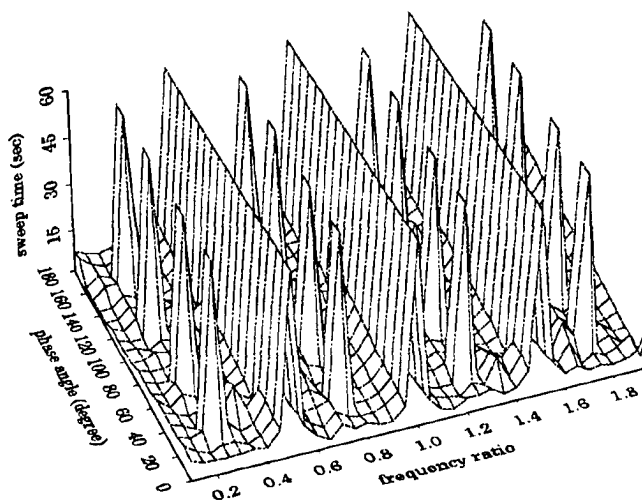
On the basis of the method described in the previous section, we investigate in this section how the sweep time required for parts engagement varies with changes in frequency ratio, phase angle, vibration frequency, insertion speed and tolerance.

The dimensions of the peg and the hole piece are given in Table 3.1:

Table 3.1 Dimensions of the peg and hole piece

radius of hole	radius of peg	width of chamfer	height of chamfer
12.7 mm	12.65 mm	2.2 mm	2.2 mm

The tolerance area, T_1 , is a circle and its diameter is equal to $2 \times [2.2 + (12.7 - 12.65)] = 4.5$ mm. The applicable tolerance T_2 is chosen as the largest rectangle within T_1 and thus T_x and T_y are both equal to $4.5/\sqrt{2} = 3.18$. In the first simulation example, we assume that the uncertainty region has the dimensions $U_x^1 = U_x^2 = U_y^1 = U_y^2 = 5.59$ mm. Therefore, the vibration amplitude $A = B = 5.59 - 3.18/2 = 4$ mm from Equation (3.3). Following the algorithm described, the sweep time required for a given ω , k and θ can be determined. For example, if frequency $\omega = 4$ rad/second, frequency ratio $k = 1.1$, phase angle $\theta = 0$, then the required sweep time is equal to 4.71 seconds.

**Figure 3.8** Sweep time vs. frequency ratio and phase angle

The required sweep time is plotted against frequency ratio k and phase angle θ in Figure 3.8. This figure shows that the plot of the sweep time is approximately symmetric with respect to frequency ratio $k = 1$ and phase angle $\theta = 90$ degrees. The highest value of the required sweep time (60 seconds) actually indicates that the tolerance area has not covered the entire uncertainty area after this amount of time (there is a possibility that the uncertainty area can never be fully covered).

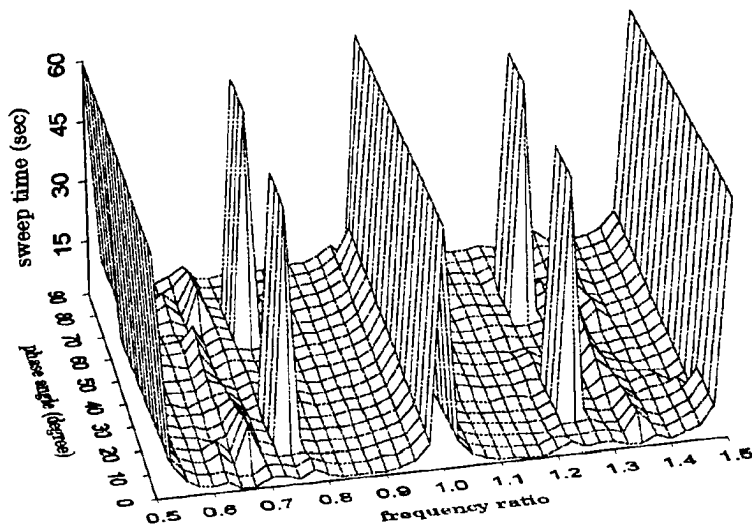


Figure 3.9 Sweep time vs. frequency ratio and phase angle

In Figure 3.9, all of the parameters are the same as those in Figure 3.8, except that the ranges of frequency ratio and phase angle are reduced. The best range of frequency ratio for smaller amount of sweep time is for k to be between 0.805 and 0.82 or between 1.18 and 1.195 as can be seen from

Figure 3.10. Let the frequency of the vibration in the x-direction is the one whose maximum is limited as described in Section 3.4, then the value of k should be larger than one. Thus the range of k for the smallest amount of sweep time in the range of 1.18 and 1.195. These figures show that the phase angle and frequency ratio are, in general, coupled in their effect on the required sweep time. However, the phase angle θ does not have much effect on the sweep time if a suitable frequency ratio is used.

We deal with the range of k between 1.05 and 1.25 and reduce the interval of k to 0.005 as shown in Figure 3.10. The optimal range of frequency ratio is seen again to be between $k = 1.18$ and 1.195. The required sweep time is the smallest at phase angle $\theta = 0$.

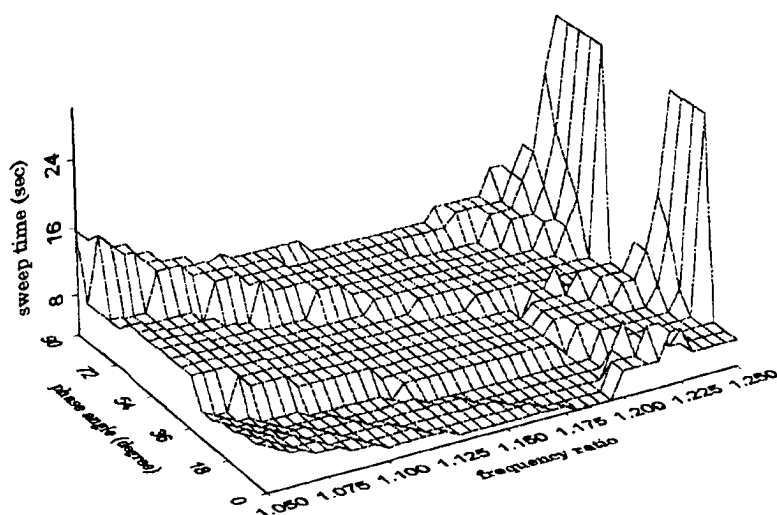


Figure 3.10 Sweep time vs. frequency ratio and phase angle

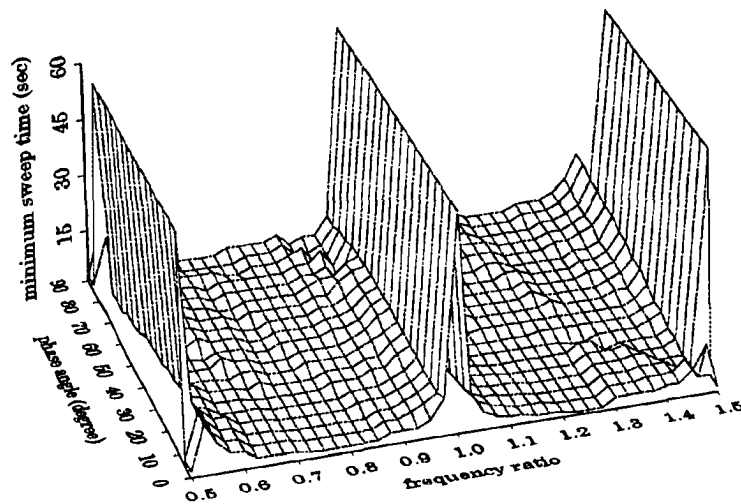


Figure 3.11 Sweep time vs. frequency ratio and phase angle ($U_x^1 = U_x^2 = U_y^1 = U_y^2 = 4.59$ mm)

The second example has the same parameter values as the first example, except that the uncertainty has the dimensions $U_x^1 = U_x^2 = U_y^1 = U_y^2 = 4.59$ mm. Figure 3.11 leads to a conclusion similar to that from the first example about the optimal frequency ratio and phase angle for engagement of the two parts. Since the uncertainty region is smaller in the second example, the best range of frequency ratio is wider than that in the first example. However, the optimal frequency ratio is still equal to about 0.810 and 1.19.

We next investigate the ratio of uncertainty to tolerance on the sweep time. To simplify the discussion, we assume that both the uncertainty set and tolerance set are rectangular boxes of the same shape, thus we can define the

ratio of uncertainty to tolerance as the ratio of either of two corresponding dimensions of the two rectangular boxes. Figure 3.12 depicts the effect of the ratio of uncertainty to tolerance on sweep time for various frequency ratios. It shows that the sweep of the tolerance region to cover the uncertainty region is difficult when the ratio of uncertainty to tolerance is high. In some cases, the uncertainty may be unknown. A value of frequency ratio should be determined and used for such a general cases. Figure 3.12 shows that if the ratio of uncertainty to tolerance is unknown, a suitable frequency ratio to use is about 1.1.

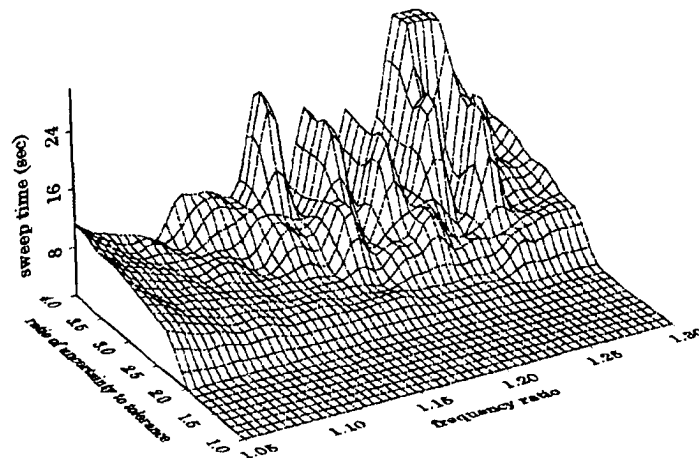


Figure 3.12 Sweep time vs. frequency ratio and ratio of uncertainty to tolerance

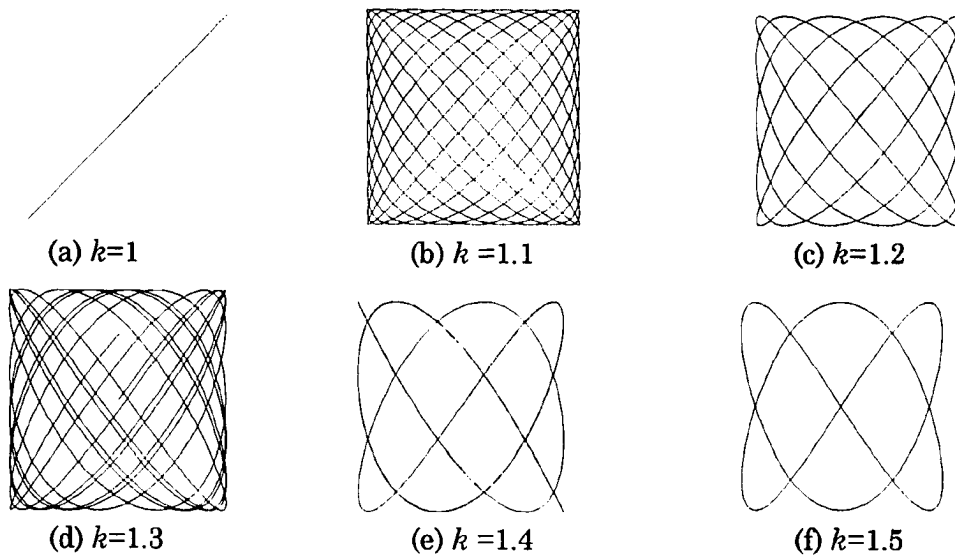


Figure 3.13 Sweep paths for different frequency ratios

Figure 3.13 shows some of the sweep paths generated by two sinusoidal motions for different frequency ratios. The value of vibration parameters is as follows: amplitude $A = B = 4$ mm, frequency $\omega = 4$ rad/sec, and phase angle $\theta = 0$. Note that vibration frequency does not affect the sweep pattern but the sweep speed. The motion is a straight line when $k=1$. This certainly is not the purpose of applying sinusoidal motion to aid parts engagement. Figures 3.13-(e) and (f) show that the sweep pattern repeats itself after 2.92 and 1.58 seconds, respectively. Obviously, they can only be applied to cases where there are large tolerances. Compared with the other cases in Figure 3.13, Figure 3.13-(b) and (c) have a smoother and better behaved sweep path. The sweep of the tolerance region can cover the whole uncertainty region faster

when $k = 1.2$ than when $k = 1.1$ if the tolerance is larger. However, $k = 1.1$ can be applied to the situation with a smaller tolerance than $k = 1.2$.

CHAPTER 4

PEG-IN-HOLE ASSEMBLY STRATEGY AND IMPLEMENTATION

4.1 Introduction

Experiments are conducted to verify the proposed algorithm determining optimal vibration parameters for minimizing engagement time and to provide further knowledge essential to the understanding of the assembly process. Some practical problems which initially cause engagement failure during experiments are solved by a force-based method. The effect of vibration parameters on contact force is also investigated.

4.2 Experimental Setup

The main experimental setup for the engagement phase of parts mating is depicted in Figure 4.1. As illustrated, a peg held at the end of an Adept One robot is to be mated with a hole mounted on the top of a positioning table, which can be moved in the x and y directions at programmed frequencies, amplitudes and phase angles to generate the desired sweep path at desired speed. The Adept-One robot is a four-degree-of-freedom robot. It is a typical SCARA robot used for assembly in industry. The positioning table is used to generate desired sweep paths. A Lord force/torque sensor mounted at the wrist is used to measure the six force and torque components throughout the assembly process. The sampling rate of this force/torque sensor is 25 Hz. A

compliant device is mounted between the peg and the force/torque sensor to increase lateral compliance. PC-1 and PC-2 are two IBM compatible personal computers. PC-1 is used to control the motion of the Adept-One robot and the sweep path of the positioning table. PC-2 is used to record the force/torque data. PC-1 and PC-2 communicate with each other in order to coordinate the whole process of peg-in-hole insertion.

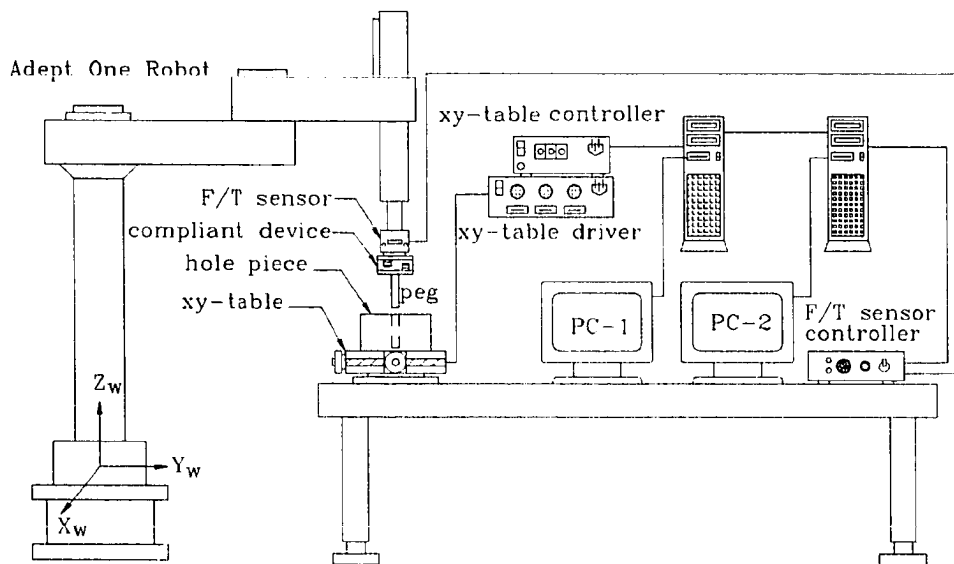


Figure 4.1 Setup for vibration-assisted mating of parts with Adept-1 robot

4.3 Practical Problems Encountered

Because the surface of the hole piece and the bottom surface of the peg may not be exactly flat or leveled, two problems causing engagement failure were encountered during the search process for engagement. These two problems are described below:

Problem 1: As shown in Figure 4.2-(a), the symbol “o” represents the contact point between the peg and the hole piece. The Adept-One robot will shut down in a few seconds (around 5 seconds) to protect the robot from damage if the force at the end-effector of the robot is greater than 280 Newtons. In our mating algorithm, the first inserting target depth of the peg is set to the level of line L_t shown in Figure 4.2-(b) so that the produced force will be smaller than 280 Newtons during the search. If the sweep direction is as shown in Figure 4.2-(b), the peg keeps in contact with the hole piece from the position 1 to the position 2. However, soon after the position 2 this contact does not exist any more. The sensor will detect that there is no contact forces in the insertion direction after the position 2 and then the peg stops at position 3 (due to the delay of the hardware response). Therefore, the sensor mistakenly regards the whole peg as being in the hole, However, although it is still not.

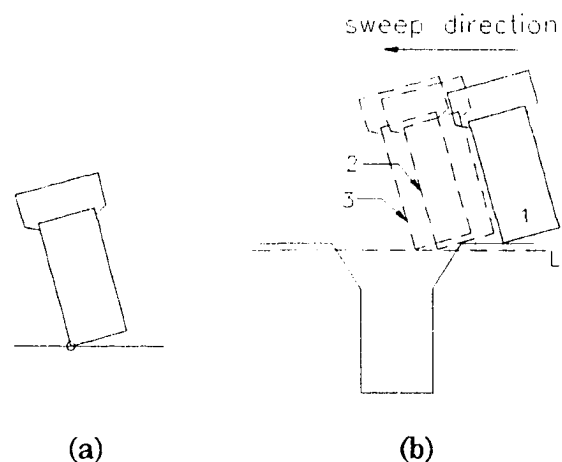


Figure 4.2 Model of problem 1

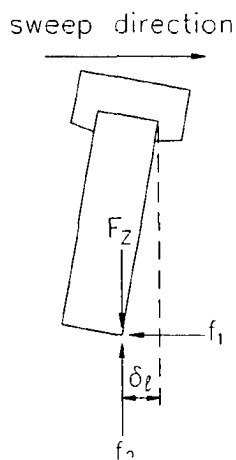


Figure 4.3 Model of problem 2

Problem 2: External forces acting on the peg's tip generated during the sweep cause the deflection of the peg. If the moving direction of the peg is from the left to the right, the peg will be inclined as shown in Figure 4.3, where F_z is the insertion force, f_2 is the reaction force, μ is the coefficient of friction, and δ_l is the lateral deflection at the peg's tip. The friction force f_1 is equal to μf_2 . The deflection of the peg relating to the force and effective compliance at the peg tip for a robot system is

$$[\delta] = [C][f] \quad (4.1)$$

where

$$[\delta] = \begin{bmatrix} \delta x \\ \delta y \\ \delta z \\ \delta \theta_x \\ \delta \theta_y \\ \delta \theta_z \end{bmatrix} = \text{deflection at the peg's tip}$$

$$[f] = \begin{bmatrix} f_x \\ f_y \\ f_z \\ m_x \\ m_y \\ m_z \end{bmatrix} = \text{external force acting on the peg's tip}$$

$$[C] = \begin{bmatrix} c_{11} & c_{12} & c_{13} & c_{14} & c_{15} & c_{16} \\ c_{21} & c_{22} & c_{23} & c_{24} & c_{25} & c_{26} \\ c_{31} & c_{32} & c_{33} & c_{34} & c_{35} & c_{36} \\ c_{41} & c_{42} & c_{43} & c_{44} & c_{45} & c_{46} \\ c_{51} & c_{52} & c_{53} & c_{54} & c_{55} & c_{56} \\ c_{61} & c_{62} & c_{63} & c_{64} & c_{65} & c_{66} \end{bmatrix} = \text{effective compliance at the peg's tip}$$

If F_z increases, f_x and μf_z increase, so is the deflection of the peg's tip. Hence, the lateral and angular errors will be increased. A way to reduce these errors is to reduce the external force. This can be achieved by reducing F_z , which can also prevent the surface of the workpiece from damage due to the larger insertion force during the sweep phase.

4.4 Algorithm of Engagement Process

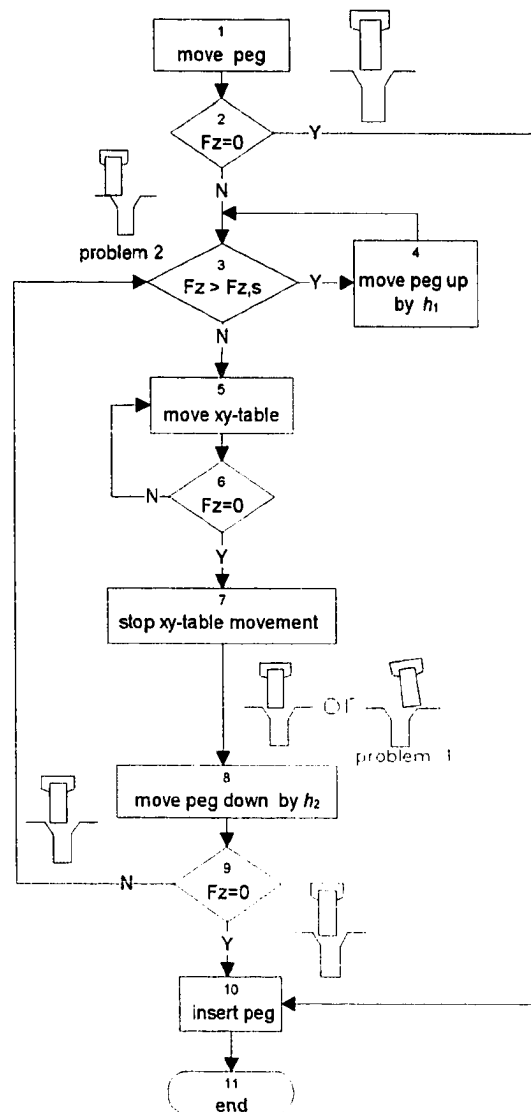


Figure 4.4 Flowchart of peg-in-hole insertion

In this experiment the insertion of the peg into the hole can be successfully performed once the peg is in contact with the chamfer because of the use of a compliant device as shown in Figure 4.1. The algorithm that has

been developed for aiding engagement is shown in Figure 4.4. This algorithm is able to solve the problems mentioned above, in addition to utilizing the sweep method described in Chapter 3.

To protect the robot system, the first inserting target point is set to a point which is a little below the surface of the hole piece. The amount below the surface of the hole piece is h_i . It was determined experimentally that moving the peg down 0.1 mm will produce around 42 Newtons of force. Since the allowable contact force in the insertion direction is 280 Newtons, h_i should be smaller than $(280 \div 42) \times 0.1 = 0.67$ mm. In Step 1 of the flowchart, the peg moves to this preset target. If the vertical force is equal to zero (Step 2), i.e., the position error is within the tolerance and then the peg keeps moving to the final target location (Step 10). If not, a decision needs to be made as shown by Step 3. If the insertion force is greater than a pre-specified safe value, $F_{z,s}$, the peg needs to move up h_i to reduce the insertion force (Step 4). This addresses Problem 2 discussed above. $F_{z,s}$ in Step 3 is the difference between the largest and smallest values of the insertion force F_z during the sweep. This difference is due to the peg contact at the different points of the surface which have different heights (mainly because the holepiece is not perfectly leveled). The largest peak-to-valley value of contact force can be determined from a simple experiment as shown in Figure 4.13. This value is the difference between the largest and smallest value of the insertion force F_z .

The amount of peg displacement h_1 in Step 4 is obtained from Equation (4.1):

$$h_1 = \delta z = c_{31}f_x + c_{32}f_y + c_{33}[f_z - (1-s)F_{z,s}] + c_{34}m_x + c_{35}m_y + c_{36}m_z \quad (4.2)$$

Since $f_x, f_y, m_x, m_y,$ and m_z are very small at the instant of contact, Equation (4.2) can be simplified to

$$h_1 = \delta z = c_{33}[f_z - (1-s)F_{z,s}] \quad (4.3)$$

where

f_z : reaction force in the insertion direction at the initial contact

$F_{z,s}$: difference between the largest and smallest value of the vertical force F_z during the hole search

s : a safe factor

The positioning table begins to move and the Lord sensor continues to measure and monitor force in Steps 5 and 6. Once the sensor detects that the insertion force is equal to zero, the positioning table stops moving (Step 7) and the peg is moved down by h_2 as shown in Step 8. The purpose of moving the peg down h_2 is to determine whether the peg really falls within the chamfer mouth and whether it will produce initial lateral and angular errors

that are too large. h_2 is the difference of the height between the lowest point and the highest point on the bottom surface of the peg, which is related to the peg's angular error, as shown in Figure 4.5.

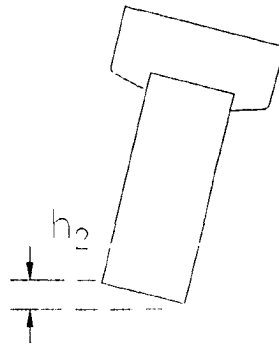


Figure 4.5 Determination of the amount of downward motion of the robot

If the vertical force is equal to zero in Step 9, i.e., the peg falls within the chamfer mouth the peg can be inserted to the final target location (Step 10). Otherwise the search process continues by going back to Step 3.

4.5 Experiments of Peg-in-Hole Insertion

Experiments of peg-in-hole insertion are performed to verify that the engagement time is less than the analytically determined required sweep time and that the proposed algorithm can deal with the practical problems mentioned in Section 4.2.

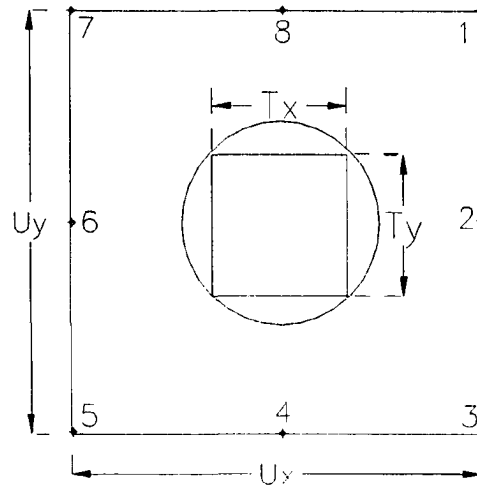


Figure 4.6 Location of initial contact points

In our experimental cases, the uncertainty area is a square, of which each side is 11.18 mm ($U_x = U_y = 11.18$ mm). The tolerance area is a circle whose diameter is 4.5 mm. The applicable tolerance area used is a square with $T_x = T_y = 3.18$ mm. The amplitudes A and B of the two vibrations in the x and y directions are equal to $(11.18 - 3.18)/2 = 4$ mm. We assume their centers of the uncertainty area and tolerance area coincide as shown in Figure 4.6. The numbers 1, 2,..., 8 in Figure 4.6 represent the initial contact positions which will be used in the experiment. The phase angle used is 0 degree, the ratio of vibration frequency is 1.1, the delay time to stop movement is 0.19 seconds, the insertion speed is 50 mm/second, chamfer angle is 45 degree, and the dimensions of the peg and the hole piece are as shown in Table 3.1. Then the vibration frequency from Equation (3.7) is:

$$\omega = \frac{2 \times [2.2 + (12.7 - 12.65)]}{0.19 \times \sqrt{4^2 + (1.1 \times 4)^2}} \cong 4 \text{ rad/sec}$$

and from Equation (3.9) is

$$\omega = \frac{50 \tan 45^\circ}{\sqrt{4^2 + (1.1 \times 4)^2}} = 8.4 \text{ rad/sec}$$

Since one half of nature frequency of the robot system is greater than these two values, the frequency of x-direction used is 4 rad/sec from Equation (3.11).

Hence, the sweep time predicted from the analysis is equal to 4.71 seconds.

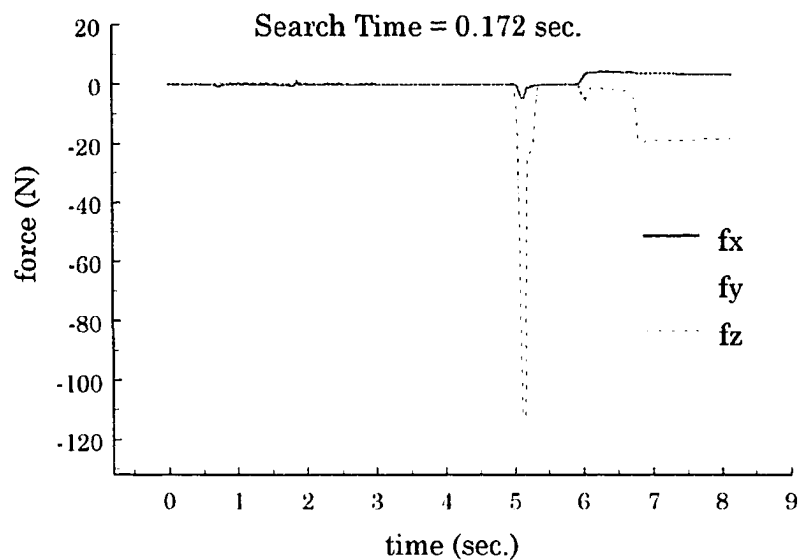


Figure 4.7 Forces with initial position at the point 5

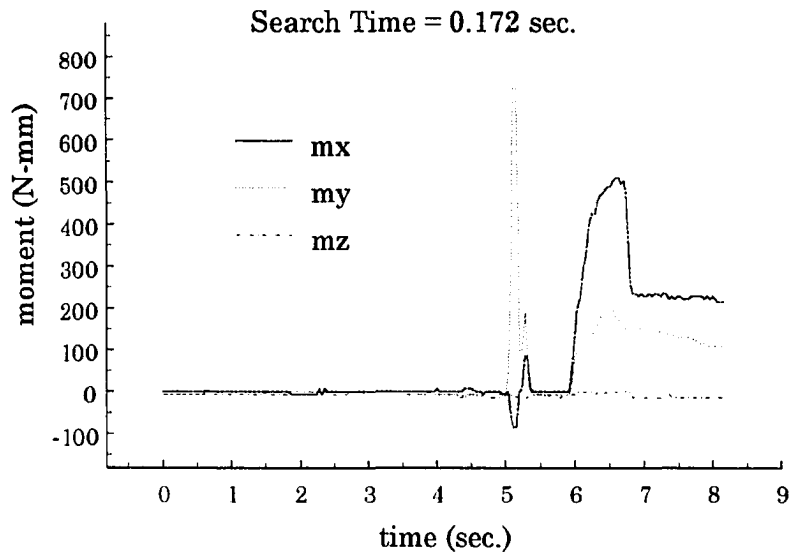


Figure 4.8 Moments with initial position at the point 5

Figures 4.7 to 4.12 illustrate the time histories of the contact and moment force during the assembly process for the above eight initial contact positions. The peak value of f_z is the contact force at the beginning of the contact. After moving up the peg by h_1 , the force becomes smaller than the safe value, and then the positioning table begins to move. The amount of upward movement of the peg depends on the value of F_z (Equation 4.3). The search time in the figures is the duration of movement of the positioning table.

In Figures 4.7 and 4.8, the contact force f_z at the beginning of contact is equal to 115 Newtons. Therefore, the peg is first moved up to reduce the contact force. The search time is only 0.172 seconds when the initial position

is at the point 5. This search time is very short compared to other initial contact positions because the moving direction of xy-table is initially toward the Point 5. Figures 4.9 to 4.12 show the results for points 3 and 8 being the initial contact points. We can see that all of f_x , f_y , m_x , and m_y have oscillatory patterns during the search motion. This is because the search motion is generated with sinusoidal motions in two orthogonal directions. Figures 4.9 and 4.11 show three and two search movements, respectively, because they have encountered the situation of problem 1 described in section 4.2. If the engagement has not succeeded yet after a search movement, the positioning table needs to move again. The experimental results for other starting points in Figure 4.6 are given in Appendix A.

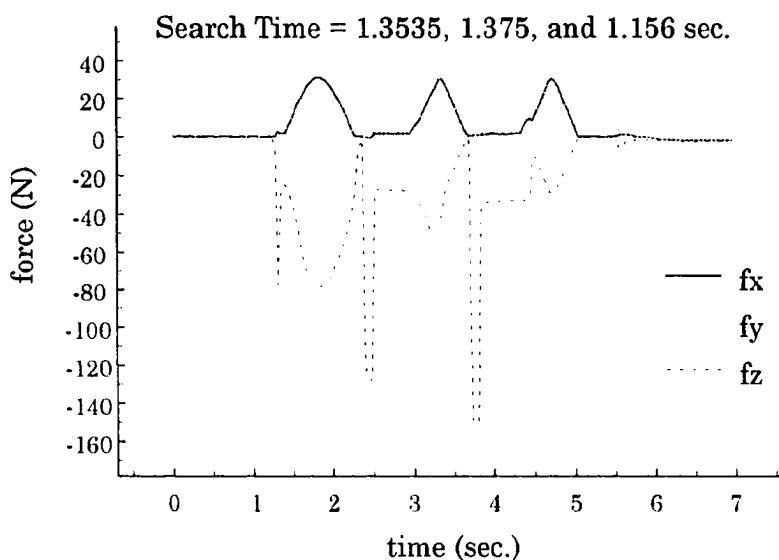


Figure 4.9 Forces with initial position at the point 3

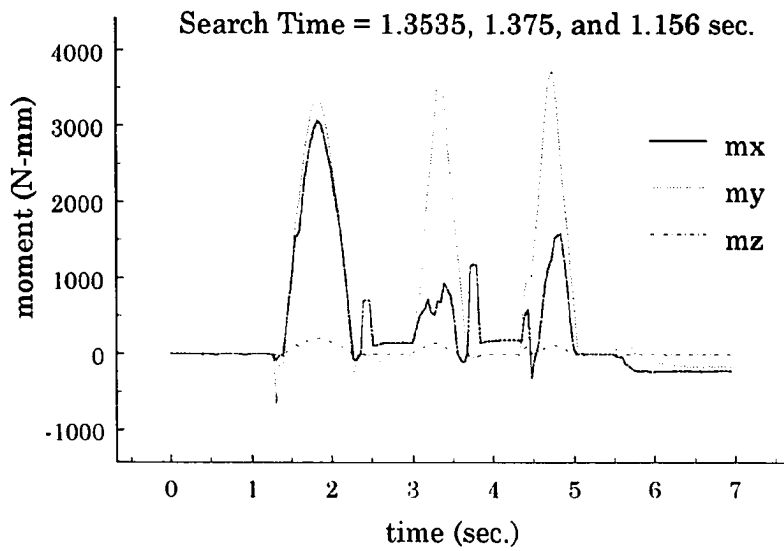


Figure 4.10 Moments with initial position at the point 3

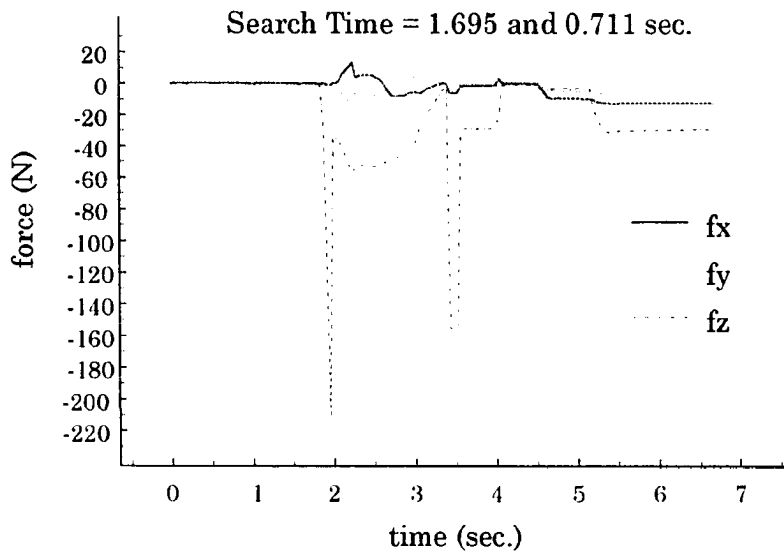


Figure 4.11 Forces with initial position at the point 8

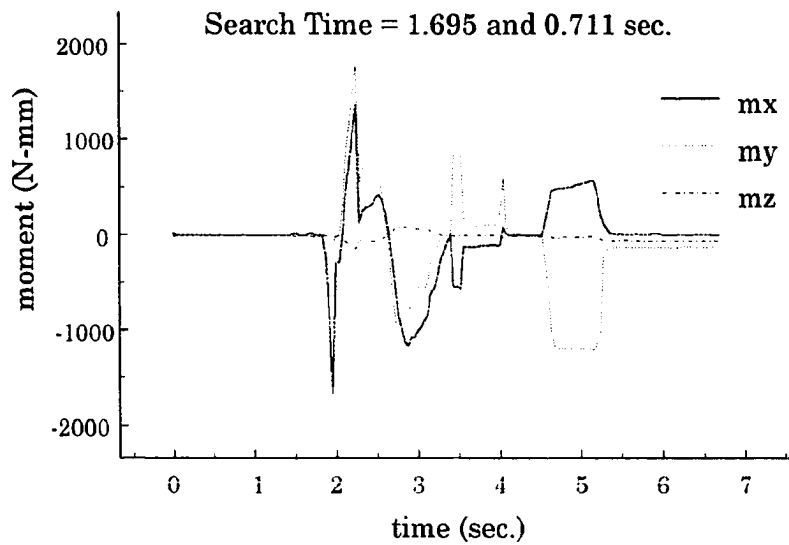


Figure 4.12 Moments with initial position at the point 8

4.6 Effect of Vibration Parameters on Contact Force

We experimentally investigate how the amplitude and frequency of vibration affect the contact force. These results provide useful information for selecting the safe value of contact force in the z-direction as mentioned in Section 4.3, and for determining the characteristics of forces in the use of vibration as an aid for parts mating. A contact force due to two orthogonal sinusoidal motions with the frequency ratio of $k = 1.1$ and the phase angle of $\theta = 0$ degree is analyzed. The sweep path is shown in Figures 3.13 (b).

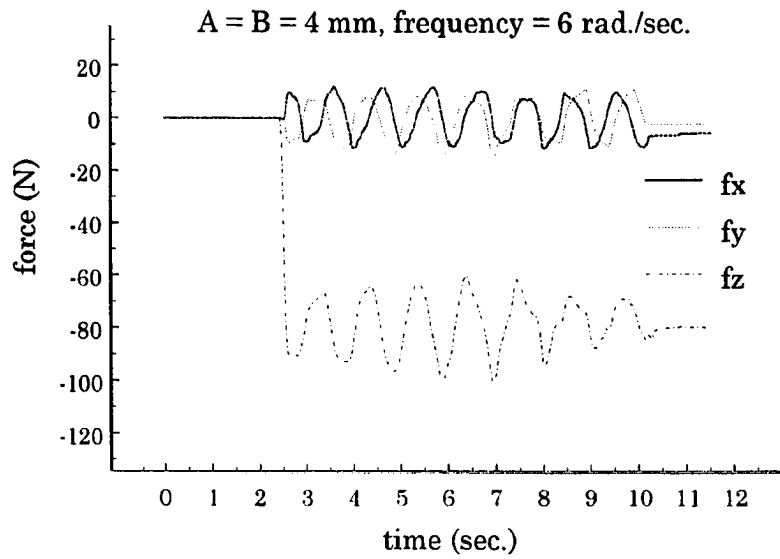


Figure 4.13 Contact forces with $A = B = 4 \text{ mm}$ and $\omega = 6 \text{ rad./sec.}$

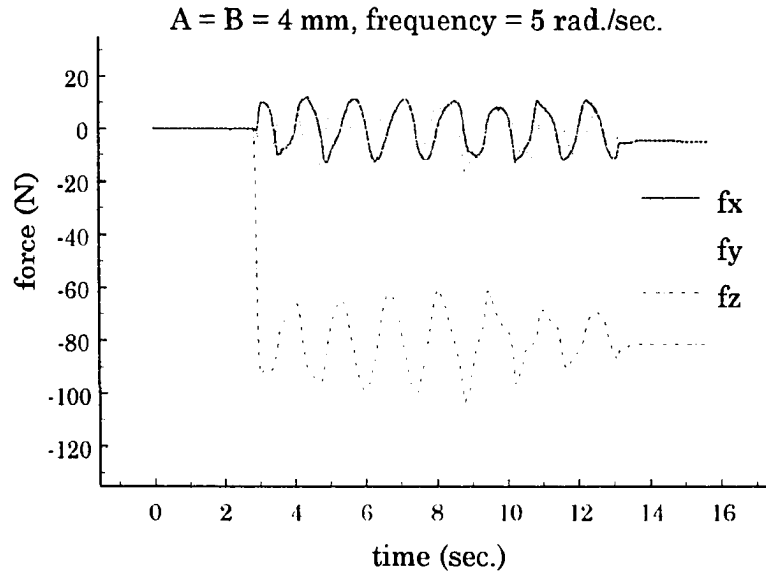


Figure 4.14 Contact forces with $A = B = 4 \text{ mm}$ and $\omega = 5 \text{ rad./sec.}$

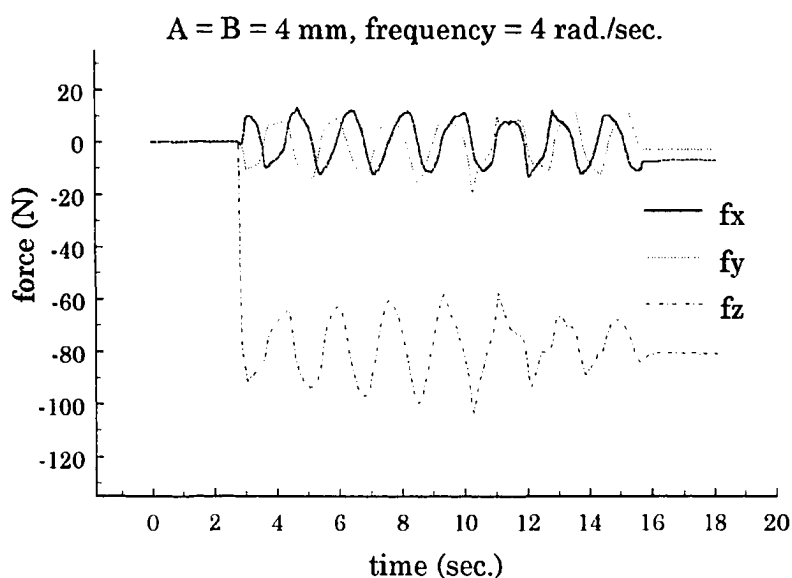


Figure 4.15 Contact forces with $A = B = 4 \text{ mm}$ and $\omega = 4 \text{ rad./sec.}$

Figures 4.13 to 4.15 show the sinusoidal sweep motions in two orthogonal directions with the same vibration amplitude, 4 mm, and the same depth in the z-direction, 0.2 mm. Their frequencies are 4, 5, and 6 radians per second, respectively. The force in the vertical direction is f_z and the friction forces in the x and y directions are f_x and f_y . Fluctuation in the amplitude of the contact force in the z-direction (f_z) can be seen. This is due to height variation of the contact point on the surface of the work piece. The largest difference of vertical force exists between 6.5 and 7 seconds in Figure 4.13. This implies that the peg sweeps from the highest point to the lowest point of the table during this duration. This difference is about 42 Newtons, which is used as a safe value in the experimental investigation as described previously. The

forces in the x and y directions also have sinusoidal patterns. The largest peak-to-peak value of f_y also occurs between 6.5 and 7 seconds, but the difference between the highest and lowest values of f_x during this period is not larger than those occurring during other periods. This implies that the peg is moving more in the y direction than in the x direction during this period. These differences provide useful information for calculating the lateral and orientation errors of the peg. Figures 4.14 and 4.15 have similar oscillating behavior as that in Figure 4.13. The variations in the contact forces during the sweep are also the same as those in Figure 4.13. They indicate that vibration speed does not affect the contact force, as expected.

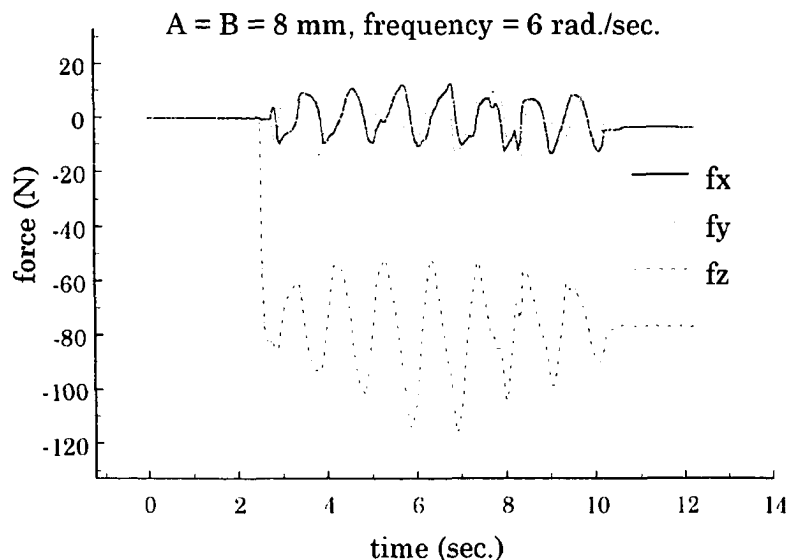


Figure 4.16 Contact forces with $A = B = 8$ mm and $\omega = 6$ rad./sec.

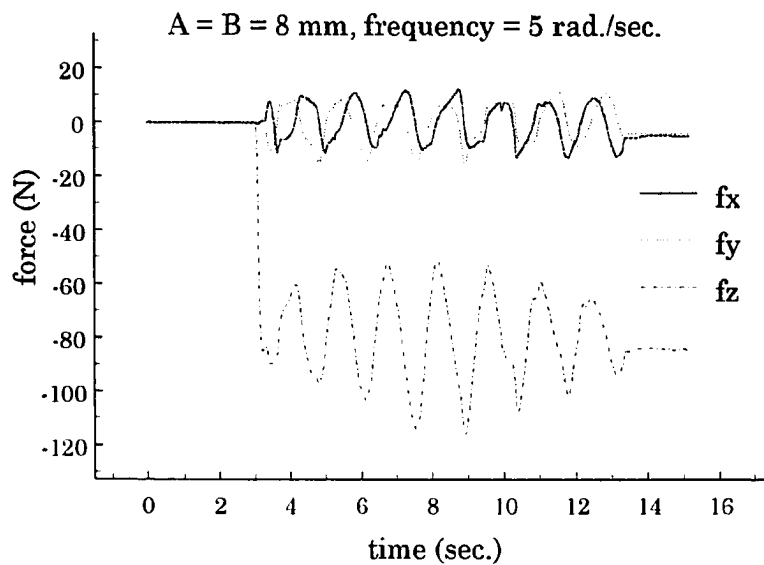


Figure 4.17 Contact forces with $A = B = 8 \text{ mm}$ and $\omega = 5 \text{ rad./sec.}$

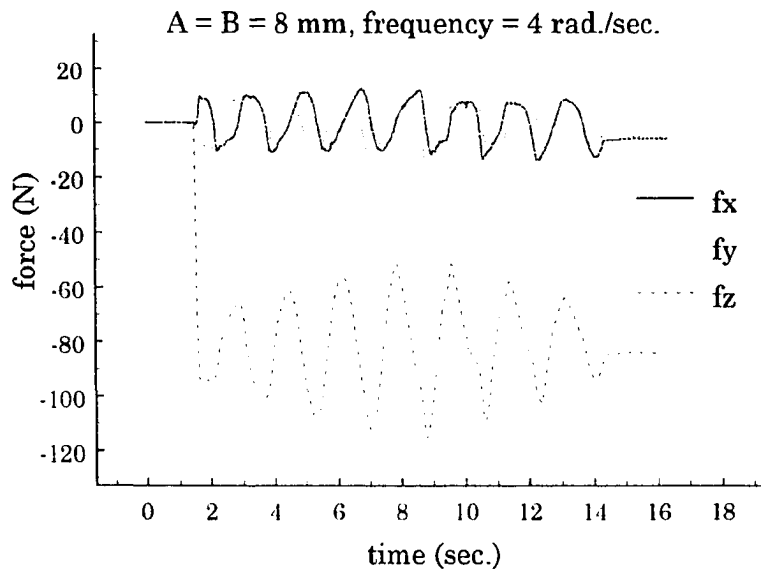


Figure 4.18 Contact forces with $A = B = 8 \text{ mm}$ and $\omega = 4 \text{ rad./sec.}$

Figures 4.16 to 4.18 have the same vibration motions as Figures 4.13 to 4.15, except that the vibration amplitude is changed from 4 mm to 8 mm. All of the curves have similar oscillatory patterns. The largest peak-to-valley value of f_z is equal to about 65 Newtons and it happens between 6.5 and 7 seconds from Figure 4.16. Figures 4.17 and 4.18 have similar oscillating curves and about the same difference of the contact forces as those in Figure 4.16. Again, these figures indicate that the vibration speed does not affect the contact force. Comparing with Figures 4.13, 4.14, and 4.15, we see that the larger the amplitude of the sweep path, the bigger the peak-to-valley value of the contact force (since the surfaces of the working parts are not perfectly leveled). The workpiece should be leveled as much as possible in robotic assembly in order to reduce the variation of the contact force, f_z , during the sweep motion and to avoid damage to part surfaces. The experiments have provided useful information pertaining to the understanding of general assembly tasks as well as showing the effect of applied vibration motion to aid parts mating.

CHAPTER 5

CONCLUSION

An impact model of robotic peg-in-hole assembly has been developed, from which the impulse and joint velocity after collision can be obtained for any robotic manipulators. Using this model we have obtained the impact equations for a SCARA robot and used them to analyze the effects of link mass, link length, joint angle, insertion speed, chamfer angle and coefficient of restitution on the impulse and departure angle when the peg impacts the chamfer surface. The information is helpful to the designer and user of a robotic assembly system in determining robot configuration, insertion speed, and other parameters to ensure assembly success without damage to mating parts. The impact equations enable the calculation of a set of joint velocities at the end of the impact. These joint velocities constitute the initial condition in the motion following the impact.

Introducing vibration to generate relative motion between two mating parts can effectively increase the tolerance of the assembly system for positional errors. This is useful for achieving engagement success when it otherwise might fail. We have analyzed the assistance of parts mating with vibrations having sinusoidal motions in two orthogonal directions. The vibration amplitudes, phase angle and ratio of vibration frequencies are

functions of the system's tolerance and uncertainty. By combining theoretical and numerical analyses, the amplitudes, frequencies, phase angles and frequency ratios of vibrations that will minimize engagement time have been obtained for general cases. Two practical problems relating to angular errors of mating parts and delay of hardware response were investigated and solved by an intelligent force-based method. Together with the optimal sweep path obtained from the analytical and numerical analyses, this method assures that engagement always succeeds within the calculated sweep time and that the vertical force does not exceed the maximum allowed during the search phase. An experimental investigation of the relationships between the contact force and vibration parameters was undertaken. The results were useful to determine safe values of contact force for successful peg-in-hole assembly.

We have not investigated the effects of vibration parameters on the mating of parts during the insertion phase. It is suggested that the research be continued along this direction in order to answer in depth the following questions:

- (1) How is the coefficient of friction affected by the amplitude, frequency and orientation of vibration during the insertion phase?
- (2) What vibration parameters can most effectively reduce the friction during insertion?

APPENDIX A

TIME HISTORIES OF FORCE AND MOMENT OF CONTACT IN THE MATING EXPERIMENT

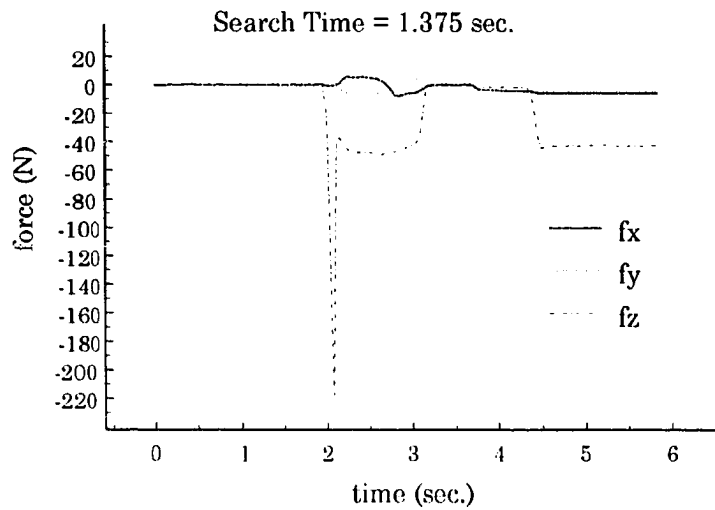


Figure A.1 Forces with initial position at the point 1

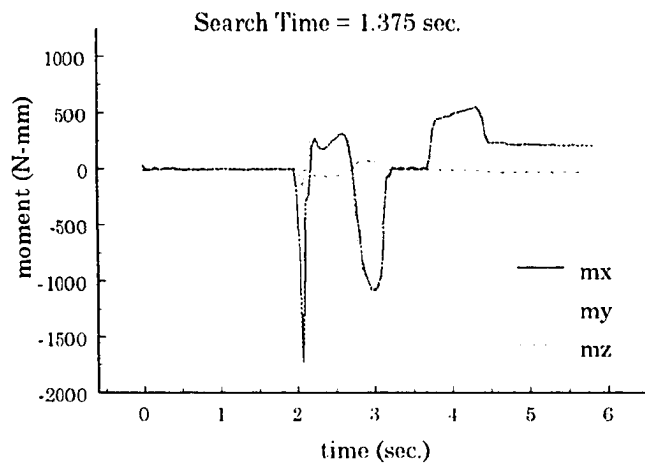


Figure A.2 Moments with initial position at the point 1

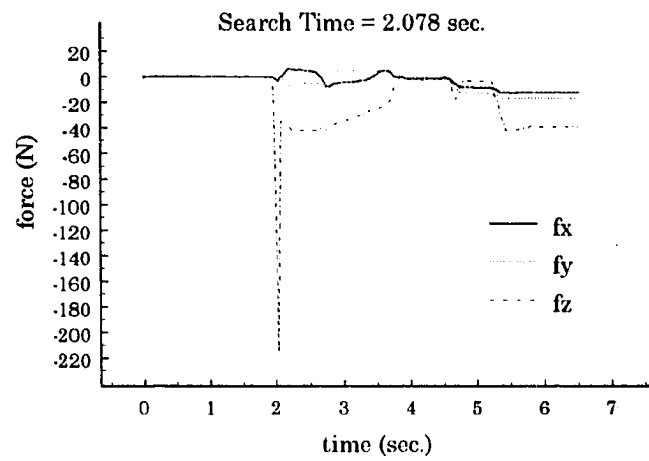


Figure A.3 Forces with initial position at the point 7

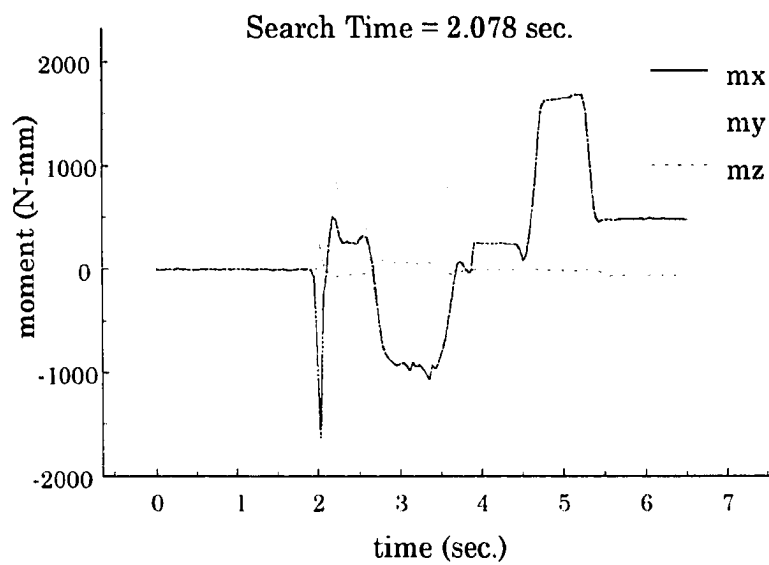


Figure A.4 Moments with initial position at the point 7

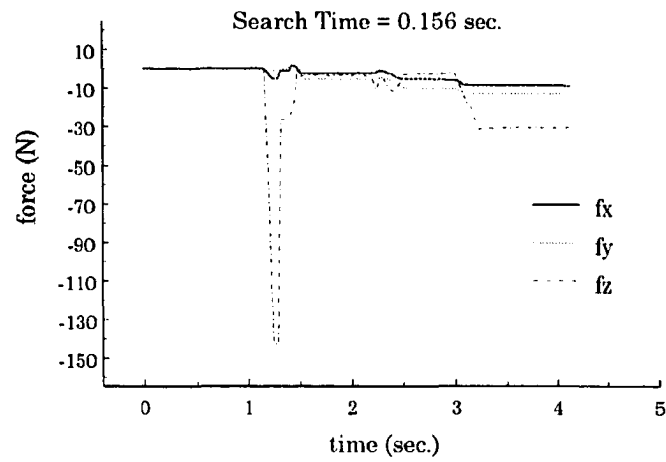


Figure A.5 Forces with initial position at the point 6

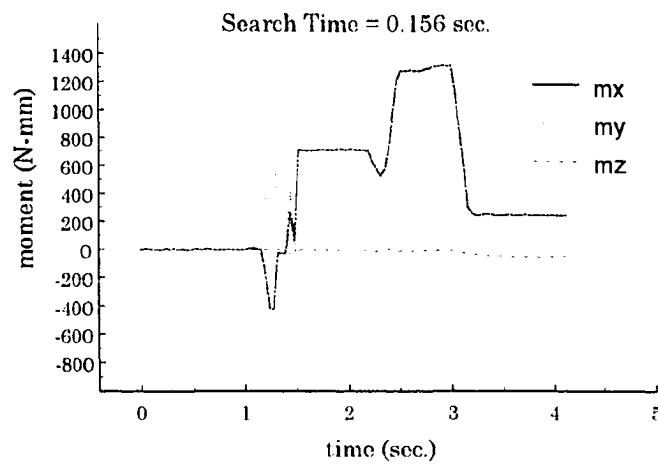


Figure A.6 Moments with initial position at the point 6

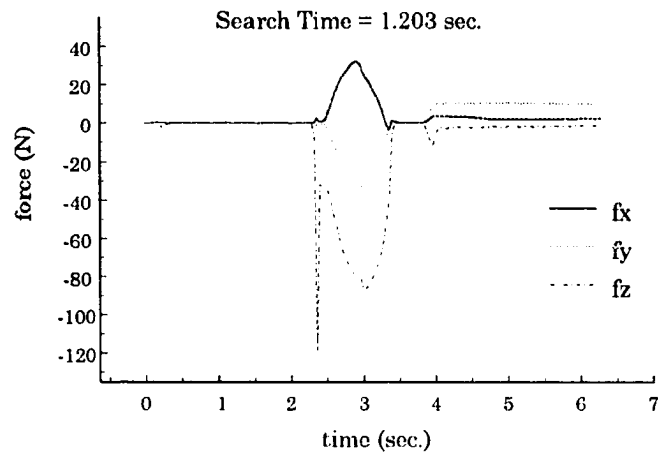


Figure A.7 Forces with initial position at the point 2

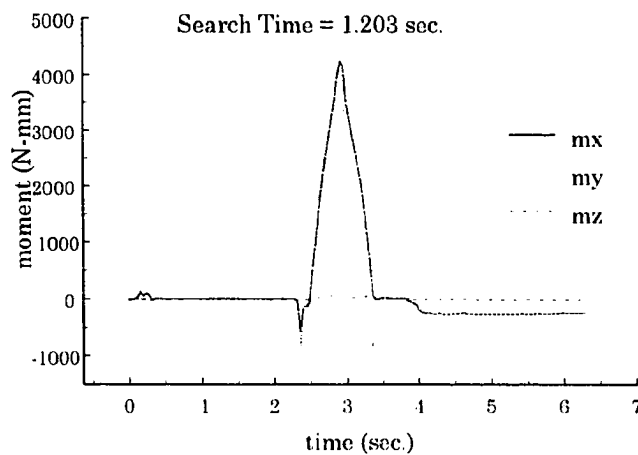


Figure A.8 Moments with initial position at the point 2

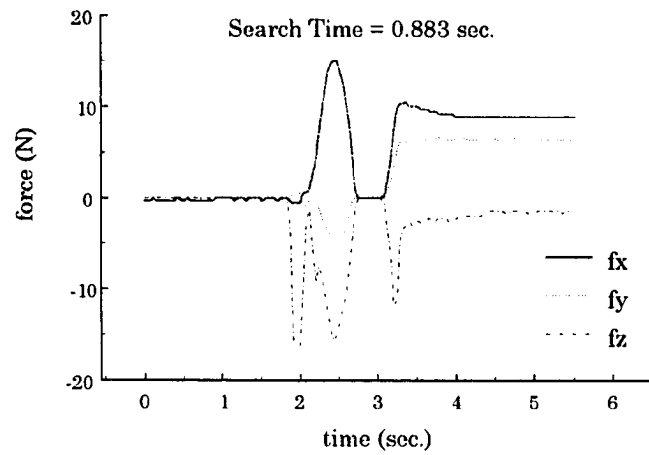


Figure A.9 Forces with initial position at the point 4

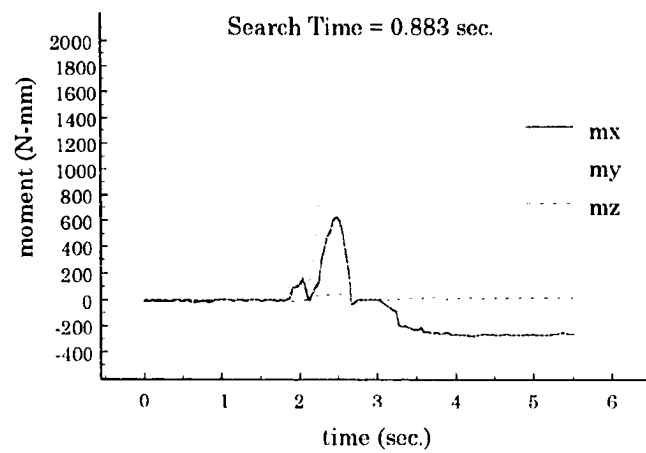


Figure A.10 Moments with initial position at the point 4

REFERENCES

- Asada, H., and Kakumoto, Y., 1988, "The Dynamic RCC Hand for High-Speed Assembly," *Proceedings of IEEE Conference on Robotics and Automation*, pp. 120-125.
- Asada, H., and Kakumoto, Y., 1990, "The Dynamic Analysis and Design of a High-Speed Insertion Hand Using the Generalized Centroid and Virtual Mass," *ASME Journal of Dynamic Systems, Measurement, and Control*, Vol. 112, pp. 646-652.
- Asada, H., and Ogawa, K., 1987, "On the Dynamic Analysis of a Manipulator and Its End Effector Interacting with the environment," *Proceeding of IEEE International Conference on Robotics and Automation*, Raleigh, NC, pp. 751-756.
- Brach, R. M., 1989, "Rigid Body Collisions," *ASME Journal of Applied Mechanics*, Vol. 56, pp. 133-138.
- Caine, M. E., Lozano-Perez, T., and Seering, W. P., 1989, "Assembly Strategies for Chamferless Parts," *Proceedings of IEEE Conference on Robotics and Automation*.
- Cutkosky, M. E., and Kao, I., 1989, "Computing and Controlling the Compliance of a Robot Hand," *IEEE Transactions on Robotics and Automation*, Vol. 5, No. 2, pp. 151-165.
- De Fazio, T. L., Seltzer, D. S., and Whitney, D. E., 1984 "The IRCC Instrumented Remote Center Compliance," *The Industrial Robot*, pp. 338-242.
- Donald, B. R., 1988, "A Geometric Approach to Error Detection and Recovery for Robot Motion Panning with Uncertainty," *Artificial Intelligence*, Elsevier Science Publishers, North-Holland, pp. 223-271.
- Drake, S. H., 1977, "Using Compliance in lieu of Sensory Feedback for Automatic Assembly," Ph. D. Thesis, MIT, Department of Mechanical Engineering, Cambridge, MA.
- Drake, S. H., Watson, P. C., and Simunovic, S. N., 1977 "High Speed Robot Assembly of Precision Parts Using Compliance Instead of Sensory Feedback," *Proceeding of the 7th International Symposium on Industrial Robots*, Tokyo, pp. 87-98.

Goldsmith, W., 1959, *Impact: The Theory and Physical Behavior of Colliding Solids*, Edward Arnold Publishers, London.

Gottschlich, S. N., and Kak, A., 1989, "A Dynamic Approach to High-Precision Parts Mating," *IEEE Transactions on Systems, Man, and Cybernetics*, Vol. 19, No. 4, pp. 797-810.

Gustavson, R. E., 1985, "A Theory for the Three-Dimensional Mating of Chamfered Cylindrical Parts," *ASME Journal of Mechanisms, Transmissions and Automation in Design*, Vol. 107, pp. 112-122.

Hara, K., and Yokogawa, R., 1991, "Application of Fuzzy Reasoning to Precision Inserting Operation," *Fuzzy Sets and System*, Elsevier Science Publishers, North-Holland, pp. 205-214.

Hoffman, B. D. Pollack, S. D. and Weissman, B., 1984, "Vibratory Insertion Process: A New Approach to Non-Standard Component Insertion," *Society of Manufacturing Engineers*, Technical Paper No. MS84-371.

Hogan, N., 1985, "Impedance Control: An Approach to Manipulation: Part I – Theory," *ASME Journal of Dynamic Systems, Measurement, and Control*, Vol. 107, pp. 1-7.

Hogan, N., 1985, "Impedance Control: An Approach to Manipulation: Part II – Implementation," *ASME Journal of Dynamic Systems, Measurement, and Control*, Vol. 107, pp. 8-16.

Huang, T. C., 1967, *Engineering Mechanics: Volume I Statics*, Addison-Wesley Publishing Company, London.

Jeong, K. W., and Cho, H. S., 1989, "Development of a Pneumatic Vibratory Wrist for Robotic Assembly," *Robotica*, Vol. 7, pp. 9-16.

Ji, Z., Leu, M. C., and Lilienthal, P. F., 1992, "Vision Based Tool Calibration and Accuracy Improvement for Assembly Robots," *Precision Engineering*, Vol. 14, No. 3, pp. 168-175.

Keller, J. B., 1986, "Impact with Friction," *ASME Journal of Applied Mechanics*, Vol. 53, pp. 1-4.

Kelly, R. B., Sood, D., and Repko, M. C., 1990, "Integrated Sensing for Circuit Board Insertion," *Journal of Robotic Systems*, pp. 487-505.

Lee, C. S. G., and Hou, E. S. H., 1988, "Automatic Generation and Synthesis of C-Frames for Mechanical Parts in an Insertion Task," *IEEE Journal of Robotics and Automation*, Vol. 4, No. 3., pp. 287-293.

Leu, M. C. and Jia, Y., 1995, "Mating of Rigid Parts by Compliant Manipulators," *ASME Journal of Engineering for Industry*, Vol. 117. pp. 240-247.

Leu, M. C. and Katz, Zvi., 1994, "Vibration-Assisted Engagement for Parts Mating," *Annals of the CIRP* Vol. 43/1/1994, pp. 27-30.

Leu, M. C. and Liu, Y., 1991, "Modeling and Analysis of Parts Mating in Vibration Assisted Compliant Assembly," *Proceeding of ASME Flexible Assembly Systems Conference*, Miami, FL, DE-Vol. 33, pp. 9-20.

Li, S. H. and Asada, H., 1992, "Robot Assembly Using a Vibratory Work Table: Optimal Tuning of Vibrators Based on the Taguchi Method," *Proceeding of Japan-USA Symposium on Flexible Automation*, Vol. 2, pp. 1531-1538.

Liao, H-T, and Leu, M. C., 1994, "Impact Model for Robotic Peg-in-Hole Insertion," *The Third Conference on Automation Technology*, Taiwan, Vol. 5, pp. 259-266.

Liu, Y. and Leu, M. C., 1991, "Design Considerations for Vibration Assisted Compliant Assembly," *Proceeding of ASME Flexible Assembly Systems Conference*, Miami, FL, DE-Vol. 33, pp. 21-29

Lozano-Perez, T., Mason, M. T., and Taylor, R. H., 1984, "Automatic Synthesis of Fine-Motion Strategies for Robots," *International Journal of Robotics Research*, Vol. 3, No. 1, pp. 3-24.

Mason, M. T., 1981, "Compliance and Force Control for Computer Controlled Manipulators," *IEEE Transactions on Systems, Man, and Cybernetics*, Vol. 11, No. 6, pp. 418-432

McCarragher, B.J., and Asada H., 1993, "Qualitative Template Matching Using Dynamic Process Models for State Transition Recognition of Robotic Assembly," *ASME Journal of Dynamic Systems, Measurement, and Control*, Vol. 115, pp. 261-269.

McCarragher, B.J., and Asada H., 1992, "A Discrete Event Controller Using Petri Nets Applied to Assembly," *Proceedings of the 1992 IEEE/RSI International Conference on Intelligent Robotics and Systems*, Raleigh, NC, pp. 2087-2094.

Mohri, N., Satio, N., and Takiguchi, M., "A New Method of Inserting Operation Applied by Ultrasonic Vibration in Assembly Process," *Proceeding of USA-Japan Symposium on Flexible Automation*, Minneapolis, MN, July 18-20 1988.

Nevins, J. L., and Whitney, D. E., 1989 *Concurrent Design of Products and Processes*, McGraw-Hill Publishers, NY.

Ohwovoriole, M. S., and Roth, B., 1981, "An Extension of Screw Theory," *Journal of Mechanical Design*, Vol. 103, pp. 725-735.

Pai, D. K. and Leu, M. C., 1991, "Uncertainty and Compliance of Robot Manipulators," *International Journal of Robotics Research*, Vol. 10, No. 3, pp. 200-213.

Peshkin, M. A., 1990, "Programmed Compliance for Error Corrective Assembly," *IEEE Transactions on Robotics and automation*, vol. 6 No. 4, pp. 473-482.

Raibert, M., and Craig, J., 1982, "Hybrid Position Force Control of Manipulators," *ASME Journal of Dynamic Systems, Measurement, and Control*, Vol. 102, pp. 65-77.

Simunovic, S. N., 1975, "Force Information in Assemblies," *Proceeding of the 5th International Symposium on Industrial Robots*, Chicago, ILL, pp. 415-431.

Sturges, R. H., Jr., 1988, "A Three-Dimensional Assembly Task Quantification with Application to Machine Dexterity," *International Journal of Robotics Research*, Vol. 7, No. 4, pp. 34-78.

Van Brussel, H., and Simons, J., 1979, "The Adaptable Compliance Concept and its Use for Automatic Assembly by Active Force Feedback Accommodation," *Proceedings of the 9th International Symposium on Industrial Robots*, Washington D.C., pp. 167-181.

Wang, Y. and Mason, M. T., 1987, "Modeling Impact Dynamics for Robotic operation," *Proceedings of IEEE Conference on Robotics and Automation*, pp. 678-685.

Watson, P. C., and Drake, S.H., 1975, "Pedestal and Wrist Force Sensors for Automatic Assembly, " *Proceedings of 5th International Symposium on Industrial Robots*, Chicago, ILL, pp. 501-511.

Whitney, D. E., 1982, "Quasi-Static Assembly of Compliantly Supported Rigid Parts," *ASME Journal of Dynamic Systems, Measurement, and Control*, Vol. 104, pp. 65-77.

Whitney, D. E., and Nevins, J. L., 1979, "What is the Remote Center Compliance (RCC) and What Can it Do ?," *Proceedings of the 9th International Symposium on Industrial Robots*, Washington, D.C., pp. 135-152.

Whitney, D. E., and Rourke, J. M., 1986, "Mechanical Behavior and Design Equations for Elastomer Shear Pad Remote Center Compliances," *ASME Journal of Dynamic Systems, Measurement, and Control*, Vol. 108, pp. 223-232.

Youcef-Toumi, K., and Gutz, D. A., 1994, "Impact and Force Control: Modeling and Experiments," *ASME Journal of Dynamic Systems, Measurement, and Control*, Vol. 116, pp. 89-98.